Characterization of New Carbosilane Liquid Crystalline Monomers and Dimers

By

Sarah Hosawi

A thesis submitted to the Department of Chemistry

In conformity with the requirements for

the degree of Master of Science

Queen's University

Kingston, Ontario, Canada

August, 2016

Abstract

'De Vries-like' smectic liquid crystals exhibit low layer contraction of approximately 1% on transitions from the SmA to the SmC phase. These materials have received considerable attention as potential solutions for problems affecting liquid crystal displays using surface-stabilized ferroelectric liquid crystals (SSFLC). In SSFLCs, layer contraction of 7−10% is normally observed during the SmA to SmC phase transition. A study by the Lemieux group has shown that liquid crystals with nanosegregating carbosilane segments exhibit enhanced 'de Vries-like' properties through the formation of smectic layers and by lengthening the nanosegregating carbosilane end-groups from monocarbosilane to tricarbosilane. This observed enhancement is assumed to be due to an increase in the cross-section of the free volume in the hydrocarbon sub-layer. To test this hypothesis, it is assumed that dimers with a tricarbosilane linking group have smaller cross-sections on time average. In this thesis, this hypothesis is tested through the characterization of new liquid crystalline monomers (**QL39-*n***) and dimers (**QL40-*n***) with 2-phenylpyrimidine cores and tricarbosilane end-groups and spacers, respectively. The thesis describes the synthesis of two homologous series of liquid crystals and their characterization using a variety of techniques, including polarized optical microscopy, differential scanning calorimetry and X-ray diffraction. The results show that the monomers **QL39-*n*** form a tilted SmC phase only, whereas the dimers **QL40-*n*** form an orthogonal SmA phase. These results are discussed in the context of our hypothesis.

Acknowledgements

I would like to thank my supervisor, Dr. Bob Lemieux for his support, patience and guidance during this project. I would also like to thank all members of the Lemieux group, and Dr. Kirk Mulligan and Dr. Chris Schubert in particular, for their assistance and valuable suggestions.

I would like to thank all of those individuals in the Chemistry Department who have helped me throughout my studies. In particular, I would like to thank Dr. Françoise Sauriol in the NMR facility, Dr. Jiaxi Wang in the mass spectrometry lab, and Kim Mackinder in the Science Store for their help.

I would like to thank Carsten Müller and Prof. Frank Giesselmann of the University of Stuttgart for performing the X-ray scattering measurements reported in this thesis.

Finally, I would like to thank my husband, Ibrahim for all his support and understanding, and my parents for their encouragement and support. I could not have completed this research project without their assistance. I would also like to thank Saudi Arabia scholarship program for their financial support during my graduate study.

TABLE OF CONTENTS

LIST OF FIGURES

LIST OF TABLES

Abbreviations

ΔH	Enthalpy of transition
Å	Angstrom
Ac	Acetyl
aq	Aqueous
C2	C2-symmetric conformer
calcd	Calculated
χ_d	Mole fraction of the dopant
Cdv	'de Vries' coefficient
cm	Centimeter
Cr	Crystalline
$d(T_{AC})$	Layer spacing at transition from SmA phase to SmC phase
dA	Layer spacing in sma phase
dC	Layer spacing in smc phase
DSC	Differential scanning calorimetry
EI	Electron impact ionization
ESI	Electrospray ionization
Et	Ethyl
Et_2O	Diethylether
EtOAc	Ethyl acetate
EtOH	Ethanol
FLC	Ferroelectric liquid crystal
h	Hours
HPLC	High performance liquid chromatography

HRMS	High resolution mass spectrometry
I	Isotropic
2-PhP	2-Phenylpyrimidine
iPr	Isopropyl
ITO	Indium-tin oxide
J	Coupling constant
kJ	KiloJoule
LC	Liquid crystal
LCD	Liquid crystal display
M	Molar
Me	Methyl
MHz	Megahertz
min	Minutes
mm	Millimeter
mol	Mole
mp	Melting point
MS	Mass spectrometry
N	Nematic
n	Director
N*	Chiral nematic
NMR	Nuclear magnetic resonance
Ph	Phenyl
Po	Reduced polarization
POM	Polarized optical microscopy

PPh$_3$	Triphenylphosphine
MgSO4	Magnesium sulfate
ppm	Part per million
Ps	Spontaneous polarization
q	Tilt angle
R	A figure of merit
rt.	Room temperature
sat	Saturated
SAXS	Small-angle X-ray scattering
SmA	Smectic A
SmA*	Chiral Smectic A
SmC	Smectic C
SmC*	Chiral Smectic C
SSFLC	Surface-stabilized ferroelectric liquid crystal
TC	Curie point
THF	Tetrahydrofuran
TOF	Time of flight
V	Volt
z	Layer normal
δ	Chemical shift
δ(T)	Chevron layer tilt angle
δ$_P$	Polarization power

Chapter 1. Introduction

Liquid crystals are materials whose properties lie between those of the conventional solid crystalline state and isotropic liquid state. At high temperatures, thermotropic liquid crystals are isotropic liquids; however, they undergo a phase transition into the liquid crystal phase when the temperature is decreased. Liquid crystals are unique and fascinating materials and have been extensively studied since their discovery in, 1888[1].

Liquid crystal materials have strong potential for technological applications; one of the most important examples is the liquid crystal display (LCD), which is firmly reliant on the liquid crystal mixtures used. Although twisted nematic LCD have attained good commercial success, they have some problems with poor response and narrow viewing angles. Scientists have been able to solve those problems through their investigations of ferroelectric liquid crystals (FLCs) as an alternative technology. Commercial FLC mixtures usually have a chiral dopant combined with an achiral liquid crystal host that has low viscosity and a broad temperature range (*vide infra*). More recent studies have focused on so-called 'de Vries-like' liquid crystals to solve the problems that decrease the quality of FLC applications[2].

In recent years, liquid crystal dimers have been employed as model compounds for semi-flexible main-chain liquid crystal polymers[3]. In this case, the term dimer refers to molecules that have two rigid mesogenic units connected via a flexible spacer such as an alkyl chain. The liquid crystal dimers can be divided into groups that are either symmetric or non-symmetric; the former includes two identical mesogenic units, whereas the latter has two different mesogenic units. In this regard, liquid crystal dimers show interesting phase behaviors that significantly differ from those of conventional low-molar-mass liquid crystals[4].

This thesis focuses on the synthesis and characterization of new liquid crystal monomers and dimers with tricarbosilane end-groups and spacers, respectively, with the aim of clarifying the relationship between their structures and properties.

1.1 Classification of Liquid Crystals

Liquid crystals are materials that exhibit the properties of both solids and liquids. Molecules that form liquid crystals are termed mesogens, and the term mesophase refers to the liquid crystal phase that is formed by these mesogens.

In general, liquid crystals can be organized into two basic classes: thermotropic and lyotropic. In a thermotropic liquid crystal, materials form mesophases in response to temperature changes in the absence of solvent. Lyotropic liquid crystals, in contrast, require the addition of solvent to form mesophases that are responsive to both thermal and concentration changes. This thesis will focus on thermotropic liquid crystals.

Typically, thermotropic liquid crystals are sub-classified depending on their molecular shape. They fall into four groups: calamitic, discotic, polycatenar, and bent-core, as shown in Figure 1-1. Calamitic liquid crystals consist of rod-shaped molecules that have rigid core units linked to flexible side chains. Discotic liquid crystals consist of disc-shaped molecules that have flat polyaromatic core units linked with multiple alkyl side chains. Polycatenar liquid crystals consist of brick- or lath-shaped molecules that have narrow rigid core units linked with multiple alkyl side chains. Bent-core liquid crystals consist of rod-like mesogens that are banana-shaped. Thermotropic liquid crystals can additionally be classified as either nonamphiphiles or amphiphiles[5]. The group of liquid crystals shown in Figure 1-1 are nonamphiphiles, but the amphiphilic liquid crystals depend on differences in the compatibility

of their molecular parts to promote ordering by microsegregation. The organosiloxane and

perfluorinated compounds shown in Figure 1-2 typify this group.

Calamitic

polycatenar
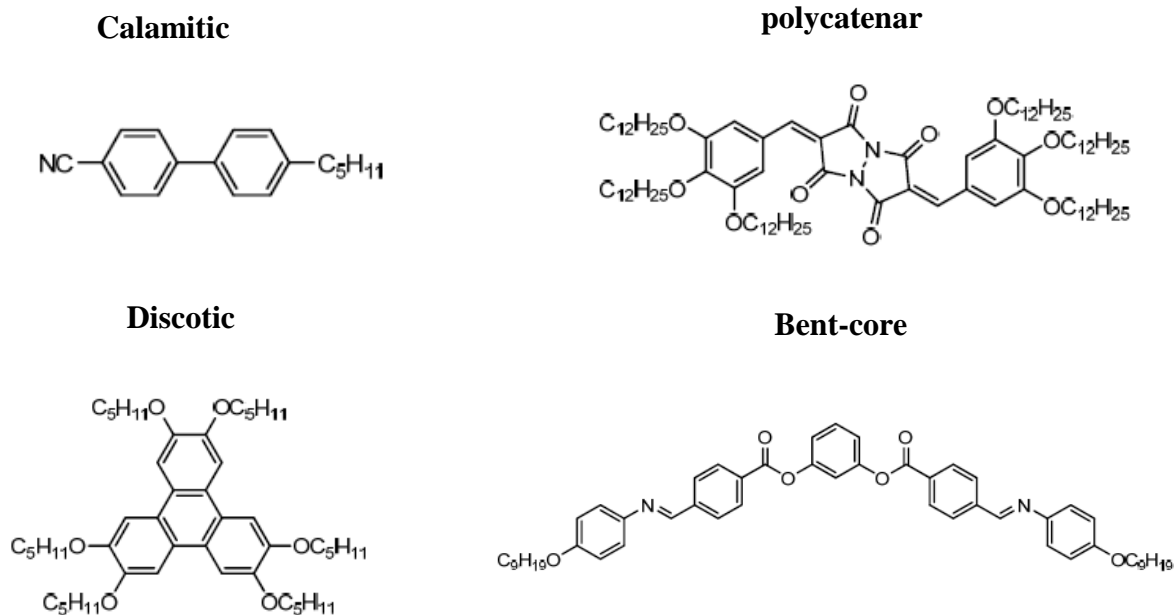
Discotic

Bent-core

Figure 1-1. Examples of calamitic, discotic, bent-core and polycatenar liquid crystals.

perfluorinated
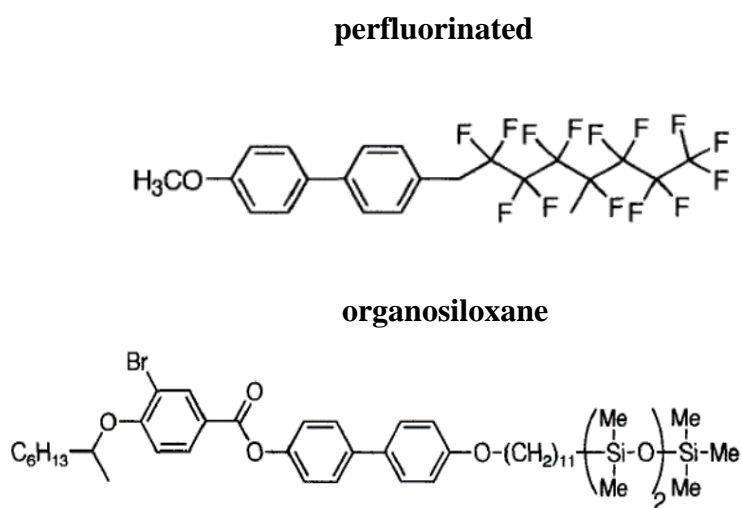
organosiloxane

Figure 1-2. Examples of perfluorinated and organosiloxane liquid crystals.

1. 2 Calamitic Mesophases

Calamitic liquid crystals are formed by rod-like molecules (mesogens). Generally, their structure contains a rigid aromatic core unit linked with one or two flexible side chains, as shown in Figure 1-3, allowing them to form a diverse range of liquid crystal phases as a function of temperature (Figure 1-4). There are two main classes of liquid crystal phases in calamitic mesogens: the nematic (N) and smectic phases. The N liquid crystalline phase shows only orientational order, whereas the smectic phases show both orientational and translational (lamellar) order. There are several smectic phases; the most important are the SmA and SmC phases, which have been used in display devices (*vide infra*).
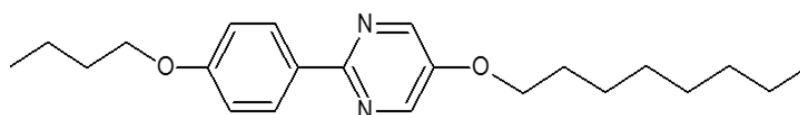
PhP1: phase sequence: Cr 58 SmC 85 SmA 95 N 98 I

Figure 1-3. 2-(4-Butoxyphenyl)-5-(octyloxy)pyrimidine a common calamitic liquid crystal and phase transition temperatures in °C[6].
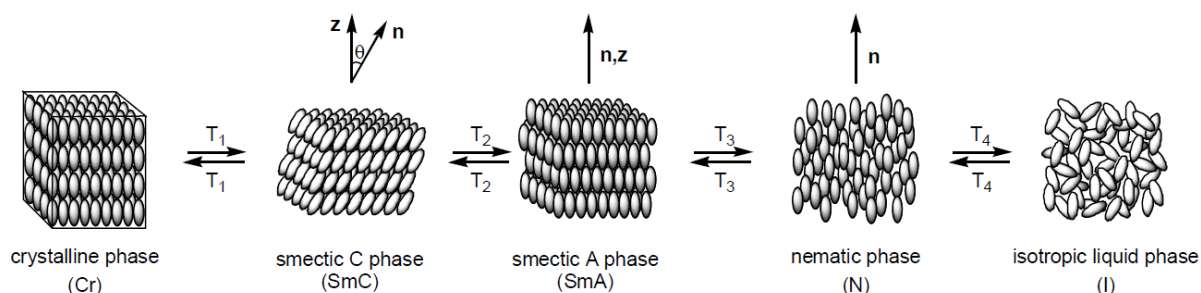
Figure 1-4. Schematic of phase transitions between crystalline, smectic C, smectic A, nematic (N), and isotropic liquid phases for a calamitic material as a function of temperature.

1.2.1 The Nematic Phase (N)

Upon cooling from a completely disordered (isotropic) liquid, the N liquid crystalline phase is the first phase observed (Figure 1-5). In the N phase, the rod-like molecules are arranged in a random positional order, but the molecular long axes are all oriented along an axis termed the director, **n**. The orientation of the N phase can be described by an order parameter, S_2, according to Equation (1.1)[7]:

$$S_2 = \frac{1}{2} < 3\ cos^2\ \theta - 1 > \qquad (1.1)$$

where θ is the angle between the long axis of the molecules and the director **n.** In the N phase, the value of S_2 is usually in the range 0.4-0.7[7], whereas $S_2 = 0$ and 1 in the disordered liquid phase and the highly ordered crystalline phase, respectively.
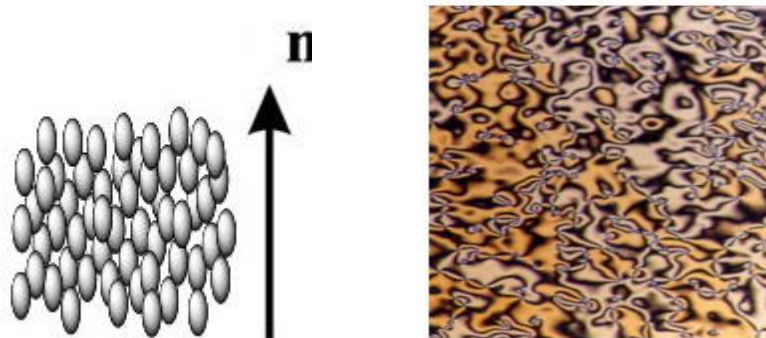
Figure 1-5: Structure of the nematic phase and characteristic Schlieren texture observed by polarized optical microscopy.

1.2.2 The Smectic A Phase (SmA)

In the SmA phase, which appears upon further cooling from the N phase, the director **n** is parallel to the smectic layer normal **z**, as shown in Figure 1-6. The layers in SmA phases are not correlated with each other and the mesogens are free to rotate around their long axes

due to the short range positional order within each layer. As the orientational order of the SmA phase is typically greater than in the N phase, the parameter S_2 usually exhibits a value of ~ 0.8. Under a polarized microscope, the SmA phase typically shows a focal conic (fan) texture and a homeotropic texture (dark regions). The homeotropic regions appear because the mesogens in the SmA phase are oriented perpendicularly to the glass slide, so no birefringence is exhibited.
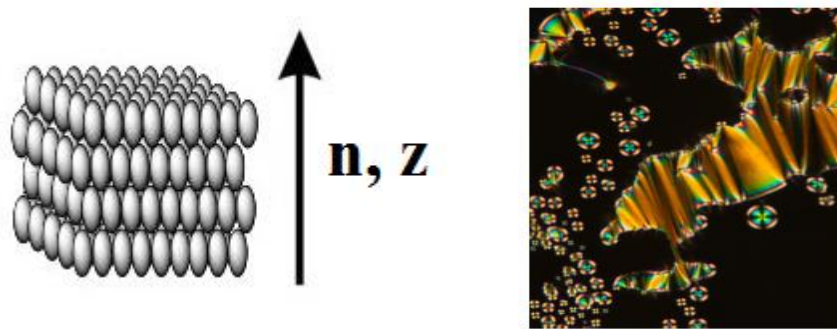
Figure 1-6: Structure of the smectic A phase and characteristic fan and homoetropic textures observed by polarized optical microscopy.

1.2.3 The Smectic C Phase (SmC)

The SmC phase is closely related to the SmA phase, and it also shows orientational and translational order. However, in the SmC phase, the molecular orientation is uniformly tilted (oriented away from the normal). The mesogen orientation **n** is tilted with respect to the layer normal **z** by a tilt angle θ, as shown in Figure 1-7; θ is normally temperature dependent and increases with decreasing temperature. In general, the SmC phase is a tilted configuration of the SmA phase. The textures formed by the SmC phase are usually described as broken fan and Schlieren textures.
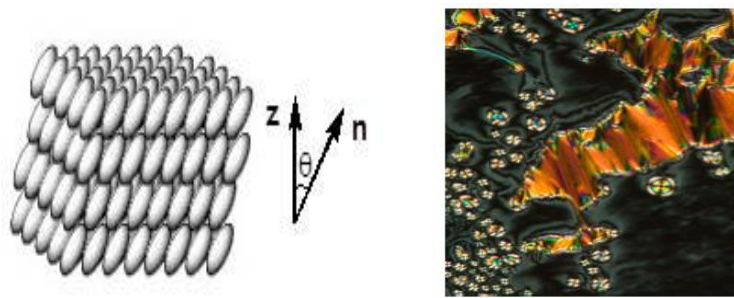
Figure 1-7: Structure of the smectic C phase and characterictic broken fan and Schlieren textures observed by polarized optical microscopy.

The models proposed by McMillan and Wulf are the most commonly used to describe the origin of the molecular tilt in the SmC phase. The McMillan model,[8] proposed in 1973, postulated that mesogens exhibiting SmC phases have polar groups such as ethers groups in both side chains linked to the core. He suggested that the formation of the SmC phase arises from the coupling of the "outboard dipoles" from the polar functional groups. The model also suggests that, upon cooling from the SmA to the SmC phase, the rotational order around the director **n** increases because of the coupling of the outboard dipoles, which leads to an induced torque, observed as tilt, in the SmC (Figure 1-8).
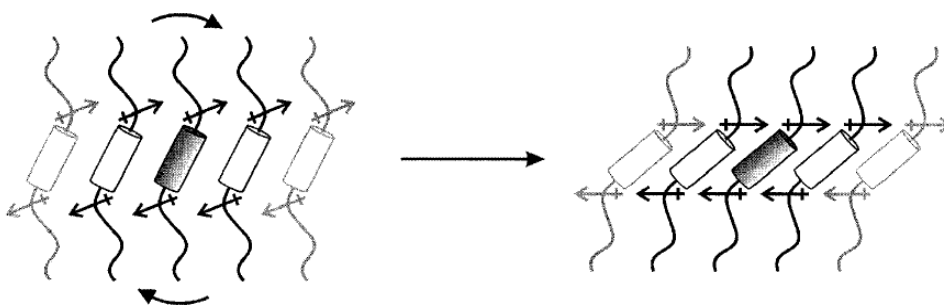
Figure 1-8: Schematic representation of the McMillan model.

However, there are some calamitic mesogens that show SmC phases without the coupling of outboard dipoles[9] on which the McMillan model is based; the Wulf model helps to explain these cases. In 1975,[10] Wulf suggested that the origin of tilt of the SmC phase depends on steric factors and packing forces. He concluded that the time-average shape of the mesogens in the SmA phase is cylindrical, which allows the molecules to rotate freely around the molecular long axis, and therefore pack vertically. In contrast, at lower temperature and after transition into the SmC phase, molecular rotation becomes more restricted around the long axis. Then, the molecules (rod-like mesogen) adopt a time-averaged zig-zag conformation that corresponds to the lowest energy conformation for calamitic molecules in the SmC phase as shown in Figure 1-9.
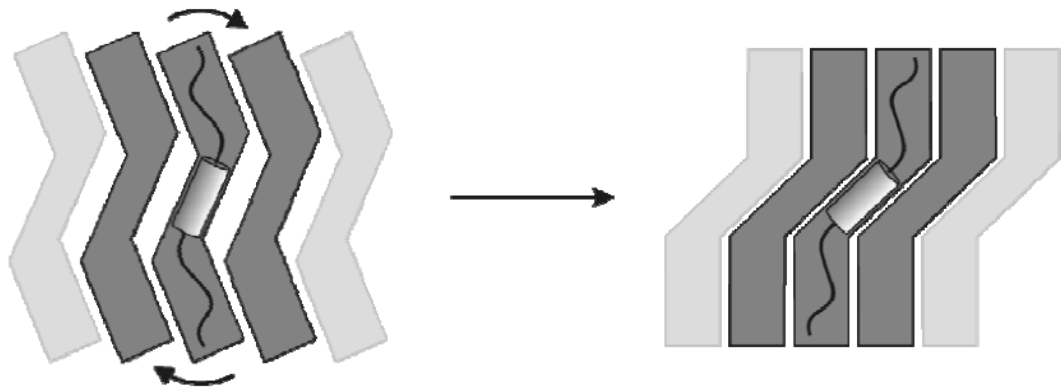
Figure 1-9: Schematic representation of the Wulf model.

1.3 Chirality in the Smectic C Phase

Liquid crystal materials are anisotropic and exhibit birefringence, an optical property in which the plane of polarized light is rotated; this property is important for technological

applications. Current research efforts are focused more on the chiral SmC phase as a light shutter, which provides several advantages[7]. These topics will be discussed in the following sections.

1.3.1 Chiral Smectic C (SmC*) Phase—Ferroelectric Liquid Crystals

The chiral SmC phase (denoted as SmC*) has the same structural features as the SmC phase. The SmC phase is biaxial, and the direction of translational order is characterized by the director **n** and layer normal **z** in the smectic tilt plane. The director **n** and layer normal **z** form a tilt angle θ. However, a chiral tilted smectic phase has additional properties that are not observed with achiral molecules, such as spontaneous polarization (P_s), which is present in the absence of an electric field. This electric polarization is known as a ferroelectric property of the SmC* phase. This property was first predicted by Meyer in 1976[11], based on the fact that SmC has two symmetry elements: a twofold rotational axis axis perpendicular to the tilt plane (C_2) and a mirror plane congruent with the tilt plane (σ) (Figure 1-10). When we move from the non-chiral SmC to the chiral SmC*, the symmetry of the phase is reduced from C_{2h} to C_2, where there is no symmetry plane. This result leads to polarization and form polar order.

However, in the absence of outside constraints, the net spontaneous polarization of the bulk material is equal to zero because the P_s vector rotates from one layer to the next in the SmC* phase to form a macroscopic helical structure, as shown in Figure 1-10. The helical structure is another chiral property of the the SmC* phase.

In 1980, Clark and Lagerwall[12] showed that when the SmC* phase is aligned between two rubbed polyimide-coated glass slides, the helical structure unwinds to give a surface-

stabilized ferroelectric liquid crystal (SSFLC) film which exhibits a net spontaneous

polarization perpendicular to the plane of the glass slides (Figure 1-11).
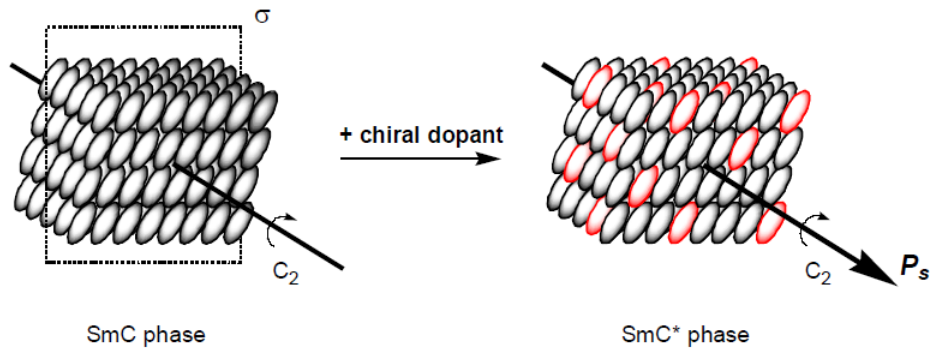
Figure 1-10. Schematic representations of symmetry elements of achiral SmC phase and

SmC* phase after chiral doping.
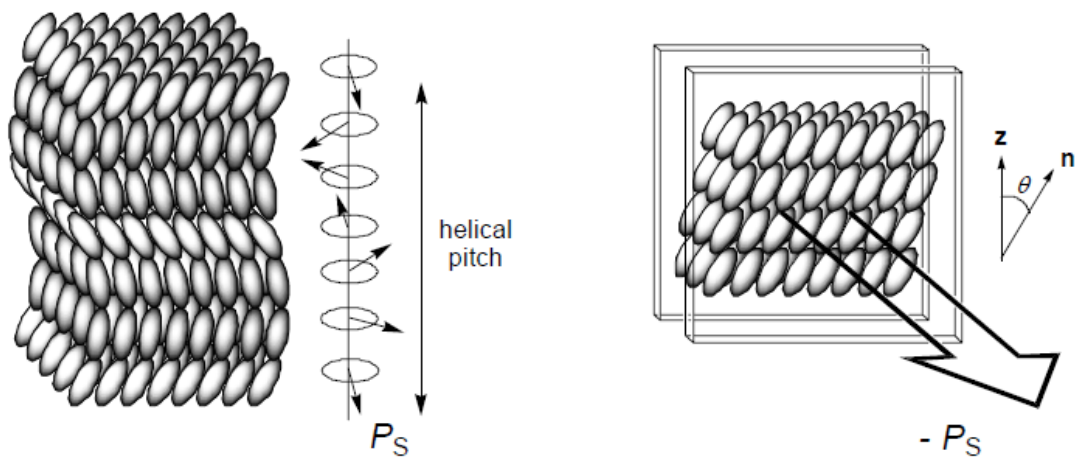
Figure 1-11. Schematic representations of macroscopic helical arrangement of SmC* phase in

bulk material (left) and in surface-stabilized state (right)[12].

Typically, LCDs work through the application of an electric field. As a result of

the birefringent properties of the LC materials, when an electric field is applied across the

SSFLC film, the LCs are switched between two opposite tilt orientations, $+\theta$ to $-\theta$, as shown in Figure 1-12, thus creating an ON/OFF light shutter between crossed polarizers .
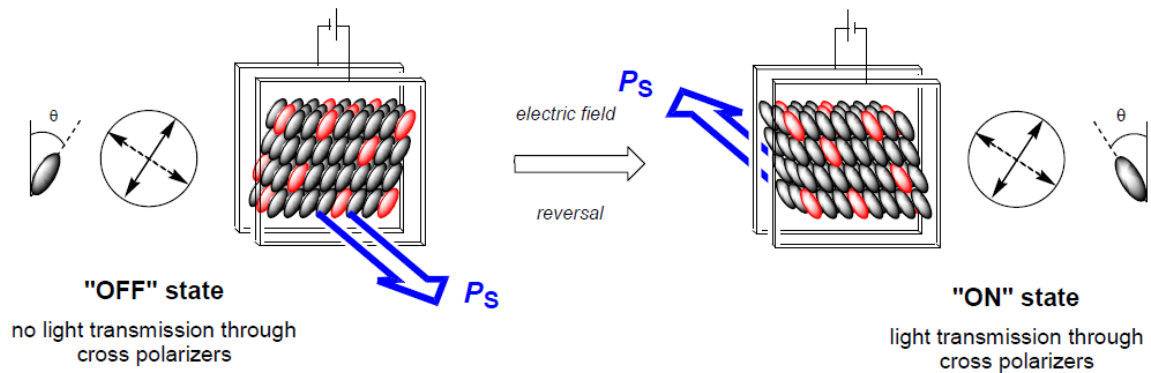
Figure 1-12. Schematic representation of ON/OFF light shutter ($+\theta$ and $-\theta$ directions) in SSFLC.

Non-chiral liquid crystal molecules are also able to present chiral structures if doped with a chiral additive. Kuszynski and Stegemeyer showed that P_s and ferroelectric properties of the chiral SmC* phase can be exhibited by dissolving a chiral dopant in a non-chiral SmC mesogenic material[13]. The design of commercial liquid crystal SmC* displays has been achieved by adding a small amount of a chiral dopant with high polarization power into an achiral, low viscosity SmC mixture[13].

SmC* materials have received much attention because the switching times achieved by SSFLC light shutters are significantly faster than those of LCDs that use nematic liquid crystals. The switching time τ between the $+\theta$ and $-\theta$ tilt orientations of a SSFLC shutter depends on the rotational viscosity (η), the applied field (E), and the P_s of the materials.[14]

$$\tau \propto \frac{\gamma \sin \theta}{P_s E} \qquad (1.2)$$

1.3.2 SSFLC Display Technology Problems

Although the SSFLC display has achieved success, it does have some drawbacks. The major problem with the application of SSFLCs is that the smectic layers usually shrink by ~7-10% during the transition from the non-tilted SmA* phase to the tilted SmC* phase when aligned between the two glass slides of the display system. As a result, a chevron geometry is formed and it is difficult to achieve the "bookshelf" configuration (Figure 1-12) in which the smectic layers are nearly parallel to the glass substrates[2]. When a SmA* phase is confined between the glass substrates of a display device, it exists in the "bookshelf" configuration. Upon cooling from the SmA* to the SmC* phase in the glass cell, the smectic layers contract, but the molecules are still anchored at the glass surfaces by the rubbed polymer substrate[2]. This results in the formation of chevron-shaped layers, folding in opposite directions with zigzag defects, as shown in Figure 1-13 b.
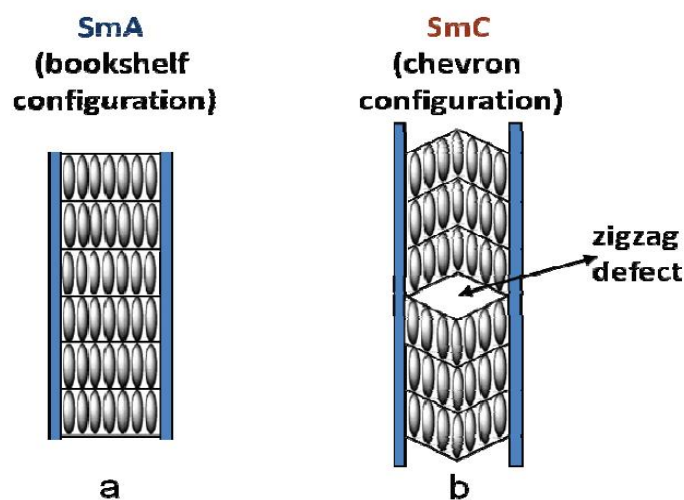
Figure 1-13. (a) The SmA* phase in the bookshelf configuration. (b) the SmC*phase in the chevron configuration[2].

In 1987,[15] Rieker and coworkers were able to experimentally confirm the presence of these chevron defects. When the chevron structures are arranged in opposite directions, they

create free volume that results in the aforementioned zigzag defects, as shown in Figure 1-14. The zigzag defects degrade the quality of an FLC device, leading to image irregularities.
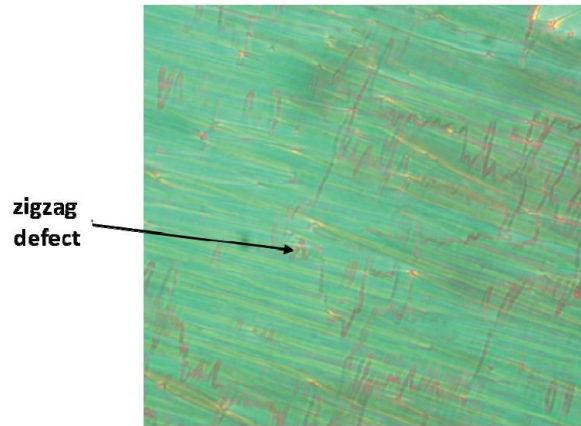
Figure 1-14. A picture of zigzag defects in a SmC* phase[2].

1.4   'de Vries-like' Materials

The problem of chevron formation and zigzag defects during the SmA−SmC transition in SSFLC devices has stimulated a great deal of research, and materials with unusually small layer contractions of less than 1% have been discovered. These materials are called 'de Vries-like'.[16,17] To explain why these molecules tilt with a small layer contraction in the SmA−SmC transition, two approaches have been considered: the diffuse cone model and the combination of low orientational order and high lamellar order.

1.4.1 De Vries Diffuse Cone Model

Initially based on the classic rigid rod model shown in Figure 1-15a, the SmA phase director **n** is oriented along the smectic layer normal **z**. Upon cooling from the SmA to the SmC

phase, the molecules are tilted from **z** by the tilt angle θ. The layer spacing of the SmC phase (d_C) is related to the layer spacing of the SmA phase (d_A) by the cosine of the tilt angle θ, as given by Equation (1.3). The layer contraction between the SmA and SmC phases, $(d_A - d_C)/d_A$, in terms of the tilt angle θ, is given by Equation (1.4).

$$d_C = d_A \cos \theta \qquad (1.3)$$

$$\frac{(d_A - d_C)}{d_A} = 1 - \cos \theta \qquad (1.4)$$
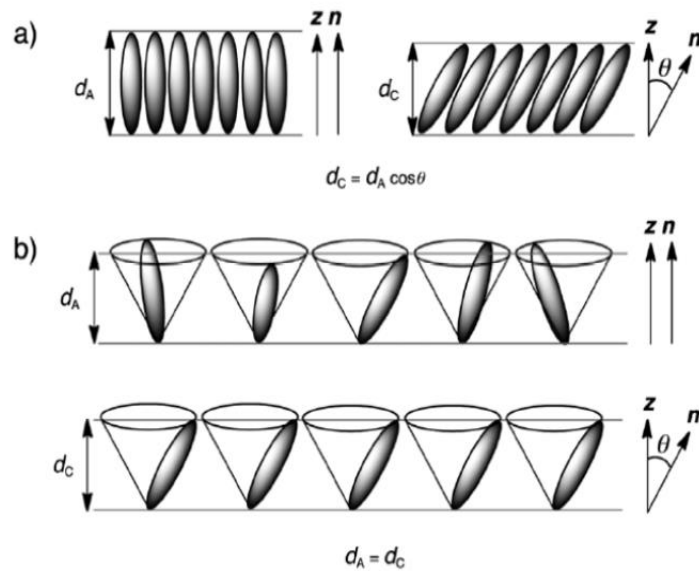
Figure 1-15. Schematic representation of the (a) rigid rod model and (b) diffuse cone model[17].

The behavior of the new 'de Vries-like' materials has been explained in a different approach via the "diffuse cone model," proposed by de Vries in 1979[17]. According to this model, the molecules in the SmA phase adopt a lamellar structure in which the molecular axes are tilted away from the director **n**, but with random azimuthal directions. Thus, there is no significant change in molecular tilt in the transition between the SmA and SmC phases, which

has been described as azimuthal ordering, as shown in Figure 1-15b. As a result, the "de Vries-like" materials have unusually small layer contractions.

The 'de Vries-like' character of a material can be measured by a reduction factor R, according to Equation (1.5). R is the ratio of the smectic tilt angle $\delta(T)$ that is required to give a layer contraction $d/d_{AC}(T)$ at a temperature T below the transfer point T_{AC} from the SmA to the SmC phase, over the optical tilt angle (θ_{opt}) measured by polarized optical microscopy (POM).[18]

$$R = \delta(T)/\theta_{opt}(T) = \cos^{-1}\big(d_C(T)\big)/d(T_{AC})\,/\theta_{opt}(T) \qquad (1.5)$$

1.4.2 Low Orientational Order and High Lamellar Order

More recently, studies by the Lemieux group[19] suggested that materials require a low orientational order parameter S_2 in order to achieve de "Vries-like" behavior. The majority of 'de Vries-like' liquid crystals have S_2 values in the range of 0.4-0.65[20], whereas these values in conventional liquid crystal SmA and SmC phases are typically ~0.7–08. In addition, 'de Vries-like' behavior has been observed for smectic layers with high lamellar order which are stabilized by nanosegregating end groups.

1.4.3 Nanosegregation

Usually, nanosegregation occurs with amphiphilic molecules, which have both hydrophilic and hydrophobic parts. The incompatible parts of these molecules tend to segregate

into distinct nanoscale domains[5]. Nanosegregation among the cores and alkyl chains in rod-shaped mesogens effectively promotes the formation of smectic layers, and end groups such as organosiloxanes and carbosilanes have been shown to promote lamellar ordering[2,21], the formation of smectic phases, and a suppression of the nematic phase. As a result of the tendency of organosiloxanes and carbosilanes, as well as hydrocarbon groups, to nanosegregate into sublayer spaces, intercalated smectic bilayers inside a lamellar structure are formed, as shown in Figure (1-16)[20,23]. The figure shows that there are three incompatible segments—the aromatic core, the alkyl chain, and the siloxane group—which give rise to the nanosegregated bilayer structure.
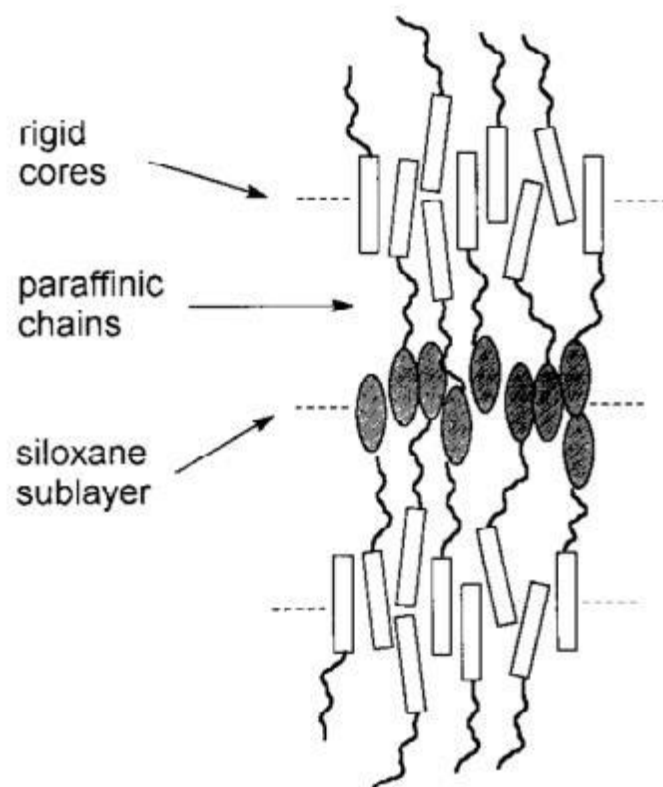
Figure 1-16. Organization of the oligosiloxane-containing liquid crystals in the smectic Layer (ref. 22).

Mesogenic materials that contain organosilicon groups are characterized by the stability of their SmC phases, which may be due to the formation of "virtual siloxane backbones" by the mesogens, because of the nanosegregation that decreases the entropic expense of the molecular tilt[20].

1.5 Examples of Known Carbosilane-Terminated 'de Vries-like' Materials

Recently, researchers have used chemically inert carbosilane end groups instead of hydrolytically labile organosiloxane end groups because the former are better suited for liquid crystal displays[20]. In recent years, the Lemieux group has developed a new design for liquid crystal mesogens which is based on the combination of a SmC-promoting element and a SmA-promoting element[20,23]. There are two examples for this design. The first is the mesogen **QL6-6**[23], which has a carbosilane end group that promotes the SmC phase by virtue of nanosegregation, as well as a chloro-terminated alkyl SmA-promoting element. Second, the mesogen **QL-16-6**[19] also has a carbosilane end group that promotes the SmC phase, in addition to a 5-phenylpyrimidine core as the SmA-promoting element. Both materials undergo a SmA–SmC transition with a layer contraction of 0.4–0.5%. The reduction factor R values for these mesogens are 0.20 and 0.17, respectively[19,23,24].

QL6-6

QL16-6
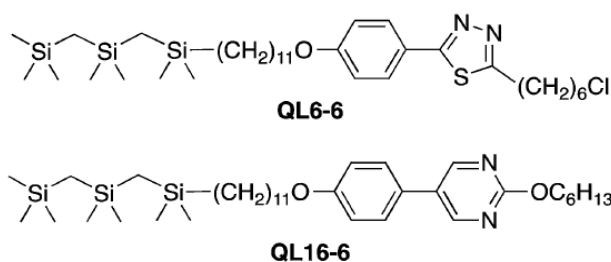
1.5.1 The Effect of Carbosilane Nanosegregation on 'de Vries-like' Properties

To investigate the connection between 'de Vries-like' properties and the length of the carbosilane end-group, a homologous series of carbosilanes was synthesized in a recent study by Lemieux group: the tricarbosilane **QL13-*n***, dicarbosilane **QL18-*n***, and monocarbosilane **QL19-*n***[19].
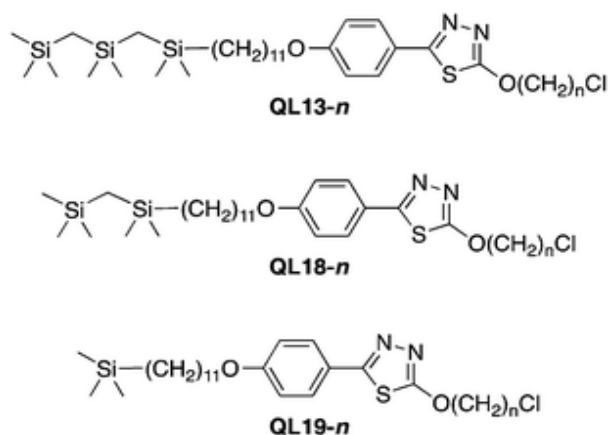
Small angle X-ray scattering (SAXS) data revealed that the 'de Vries-like' behavior depends on the length of the nanosegregating carbosilane end group, and increases from the monocarbosilane to the tricarbosilane. Nanosegregation was the key to observing any 'de Vries-like' behavior in these materials. In addition, the results showed that the nanosegregating carbosilane end groups created high lamellar ordering, which was also required to achieve 'de Vries-like' behavior. The shortening of the carbosilane length reduced the lamellar ordering of the mesogens, which was indicated by the reduction factor R and the change in layer spacing (Figure 1-17). The reduction factor R increased with the decrease in the length of the nanosegregating carbosilane end groups in these mesogens.
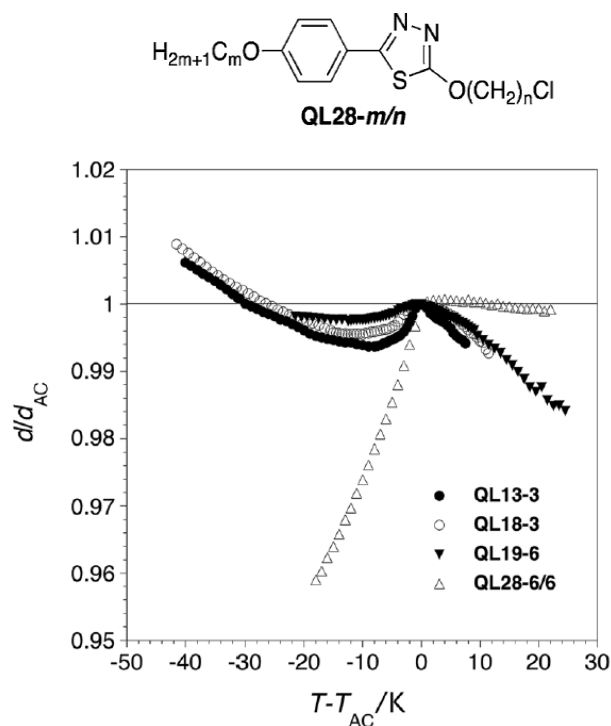
Figure 1-17. Smectic layer spacing d/d_{AC} versus the reduced temperature $T - T_{AC}$ for mesogens **QL13-3**, **QL18-3**, **QL19-6**, and **QL28-6/6** (from ref. 19).

From 2D X-ray scattering analyses of monodomains, the orientational order (S_2) was found to be influenced by the length of the carbosilane end group: S_2 decreases with increasing length of the carbosilane end group, as shown in Figure 1-18. There is a small change in S_2 between **QL28-6/6** and **QL19-6**, but S_2 decreases significantly between **QL19-6** and **QL18-3** or **QL13-3**, as shown in Table 1-1. The low orientational order that is also required to achieve 'de Vries-like' behavior in these materials supports the hypothesis that increasing 'de Vries-like' behavior requires high lamellar order and low orientational order. However, we still do not understand why orientational order decreases with increasing length of the carbosilane end-group.
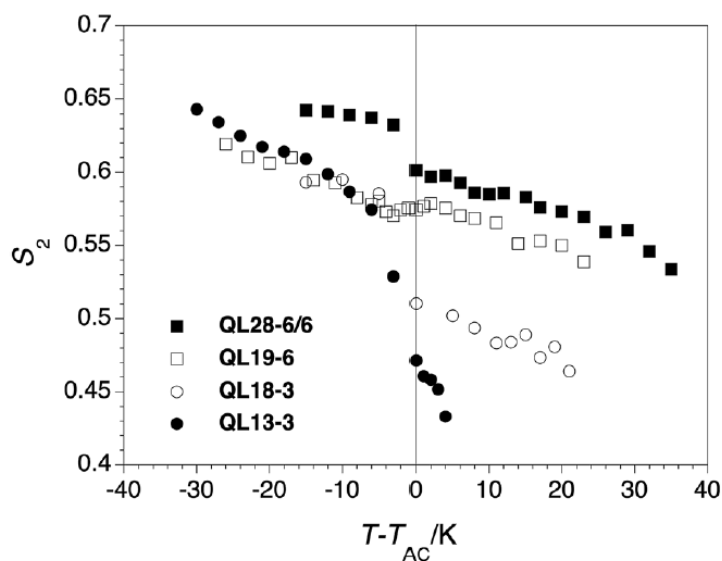
Figure 1-18. Orientational order parameter (S_2) versus reduced temperature $T - T_{AC}$ for mesogens **QL13-3**, **QL18-3**, **QL19-6**, and **QL28-6/6** (from ref. 19).

Table 1-1. Liquid crystal layer d_{AC} spacings, orientational order parameter S_2 and reduction factor R at $T - T_{AC} = -10$ K.

Compound	d_{AC} / Å	S_2	R
QL13-3	42.8	0.47	0.25
QL18-3	40.2	0.51	0.32
QL19-6	39.7	0.57	0.39
QL28-6/6	27.4	0.60	1.0

1.5.2 Hypothesis

From previous study of the effect of carbosilane nanosegregation on 'de Vries-like' properties, one can assume that the tricarbosilane end-group is approximately spherical in shape as a result of shallow torsional energy profiles. Therefore, in the intercalated bilayer structure formed by carbosilane-terminated mesogens, nanosegregation may produce a significant amount of free volume in the hydrocarbon sub-layer, which would be "backfilled"

20

by an increase in orientational fluctuations to minimize the free energy. The requirement for such orientational fluctuations would be decreased for the mono- and dicarbosilane end groups due to their smaller steric bulks compared to the tricarbosilane, as depicted in Figure 1-19. This is consistent with the orientational order parameter S_2 being inversely proportional to the length of the carbosilane end group (see Table 1-1).
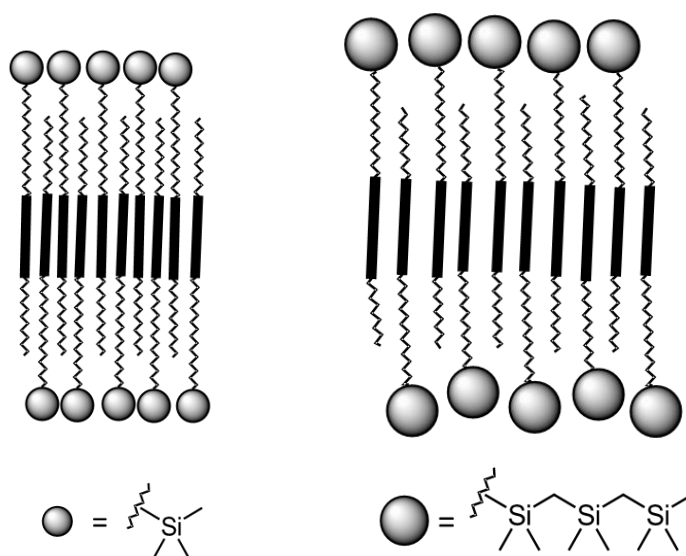
Figure 1-19. Schematic representations the bulky size of the monocarbosilane end-group (left) and tricarbosilane (right).

1.5.3 Test of Hypothesis

To test this hypothesis, we have investigated the effects of reducing the free volume in the intercalated bilayers of a series of tricarbosilane dimers (**QL40-n**) by comparing their properties to those of the corresponding monomers (**QL39-n**), including measurements of S_2. We assume that the dimers with the tricarbosilane "spacer" will form intercalated bilayers similar to those shown in Figure 1-19. However, in this case, the spacer will be forced into more extended conformations by the lamellar ordering of the two mesogenic units extending

in opposite directions along the layer normal **z**, which should result in a smaller time-average cross-section[25].

1.6   Project Outline

The purpose of this project is to test the hypothesis and investigate the mesogenic properties of the model tricarbosilane dimers **QL40-*n*** using the **2-PhP** mesogenic scaffold, for comparison with the mesogenic monomers **QL39-*n***, with the ultimate objective of understanding the origin of 'de Vries-like' behavior in carbosilane-terminated mesogens. This thesis describes the synthesis of the liquid crystals and their characterization by polarized microscopy, DSC measurements and X-ray scattering experiments.

$$-Si\frown Si\frown Si-(CH_2)_{11}-O-\text{Ar}-O-C_nH_{2n+1}$$

QL39-*n*, n=5-10

$$C_nH_{2n+1}-O-\text{Ar}-O-(CH_2)_{11}-Si\frown Si\frown Si-(CH_2)_{11}-O-\text{Ar}-O-C_nH_{2n+1}$$
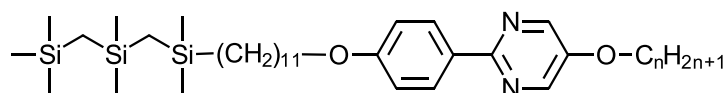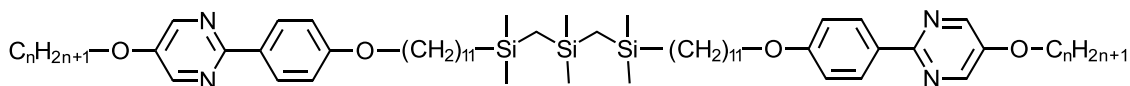
QL40-*n*, n=5-10

1.7 References

(1) Reinitzer, F. *Monatsh. Chem.***1888**, *9*, 421.

(2) Lagerwall, J. P. F.; Giesselmann, F. *ChemPhysChem* **2006**, *7*, 20-45.

(3) Demus, D.; Goodby, J.; Gray, G. W.; Spiess, H. W.; Vill, V. *Handbook of Liquid Crystals, Volume 7: Liquid Crystal Dimers and Oligomers*, 1998.

(4) Imrie, C. T. *Liquid Crystals II, Volume 95: Liquid Crystal Dimers*, 1999.

(5) Tschierske, C. *J. Mater. Chem.* **1998,** *8,* 1485-1508.

(6) Vizitiu, D.; Lazar, C.; Halden, B.; Lemieux, R. *J. Am. Chem. Soc.* **1999**, 121(36), 8229-8236.

(7) Demus, D.; Goodby, J.; Gray, G. W.; Spiess, H. W.; Vill, V. *Handbook of Liquid Crystals, Volume 2A: Low Molecular Weight Liquid Crystals I*, 1998.

(8) McMillan, W. L. *Phys. Rev. A* **1973,** *8 ,* 1921.

(9) Goodby, J. W.; Gray, G. W.; McDonnell, D. G. *Mol. Cryst. Liq. Cryst.* **1977**, *34*, 183.

(10) Wulf, A. *Phys. Rev. A* **1975**, *11*, 365.

(11) Meyer, R. B.; Liebert, L.; Strzelecki, L.; Keller, P. *J. Phys. (Paris), Lett.* **1975**, *36*, L69-L71.

(12) Clark, N. A.; Lagerwall, S. T. *Appl. Phys. Lett.* **1980**, *36*, 899.

(13) Kuczynski, W.; Stegemeyer, H. *Chem. Phys. Lett.* **1980**, *70*, 123-126.

(14) Handschy, M. A.; Clark, N. A.; *Appl. Phys. Lett.* 1982, 41, 39.

(15) Rieker, T. P.; Clark, N. A.; Smith, G. S.; Parmer, D. S.; Sirota, E. B.; Safinya, C. R. *Phys. Rev. Lett.* **1987**, *59*, 2658-2661.

(16) De Vries, A. *Mol. Cryst. Liq. Cryst.* **1977**, *41*, 27-31.

(17) De Vries, A. *J. Chem. Phys.* **1979**, *70*, 2705.

(18) Radcliffe, M. D.; Brostrom, M. L.; Epstein, K. A.; Rappaport, A. G.; Thomas, B. N.; Shao, R.; Clark, N. A. *Liq. Cryst*. **1999**, *26*, 789-794.

(19) Mulligan, K. M.; Bogner, A.; Song, Q.; Shubert, P. J.; Giesselmann, F.; Lemieux, R. P. *J. Mater. Chem. C* **2014**, *2*, 8270.

(20) Song, Q.; Nonnenmacher, D.; Giesselmann, F.; Lemieux, R. P. *J. Mater. Chem. C* **2013**, *1,* 343.

(21) Shoosmith, D.; Carboni, C.; Perkins, S.; *Mol. Cryst. Liq. Cryst. Sci. Technol., Sect. A.* **1999**, *331*, 2041.

(22) Ibn-Elhaj, M.; Skoulios, A.; Guillon, D.; Newton, J.; Hodge, P.; Coles, H. *J. Liq. Cryst.* **1995**, *19*, 373.

 (23) Song, Q., Bogner, A., Giesselmann, F., & Lemieux, R. P. *Chem. Commun.* **2013**, 49, 8202.

(24) Schubert, C. P.; Bogner, A.; Porada, J. H.; Ayub, K.; Andrea, T.; Giesselmann, F.; Lemieux, R. P. *J. Mater. Chem. C* **2014**, *2*, 4581.

(25) Robinson, W. K.; Carboni, C.; Kloess, P.; Perkins, S. P.; Coles, H. J. *Liq. Cryst.*, **1998**, *25*, 301.

(26) Lemieux, R. P. http://faculty.chem.queensu.ca/people/faculty/lemieux/Research.asp

Chapter 2. 2-Phenylpyrimidine Monomeric and Dimeric Tricarbosilane Liquid Crystals

2.1 Syntheses

The synthesis of the monomeric series **QL39-*n*** was carried out by selective alkylation of 2-(4-hydroxyphenyl)pyrimidin-5-ol (**1**), which is commercially available, with the appropriate alcohols via Mitsunobu reactions to give **2-*n*** (Scheme 2-1). A second alkylation with 1-bromo-12,12,14,14,16,16-hexamethyl-12,14,16-trisilaheptadecane gave **QL39-*n*** in 80-95% yield. Alternatively, alkylation of **2-*n*** with 10-undecen-1-ol via a Mitsunobu reaction gave **3-*n*,** which was converted to **QL39-*n*** via a platinum-catalyzed hydrosilation reaction using 1,1,1,3,3,5,5-heptamethyltrisilane and Karstedt's catalyst. The synthesis of the dimeric series **QL40-*n*** was carried out by alkylation of **2-*n*** with 1,27-dibromo-12,12,14,14,16,16-hexamethyl-12,14,16-trisilaheptacosane in 42-60% yield, as shown in Scheme 2-1. The monomers and dimers compounds were recrystallized from ethanol.
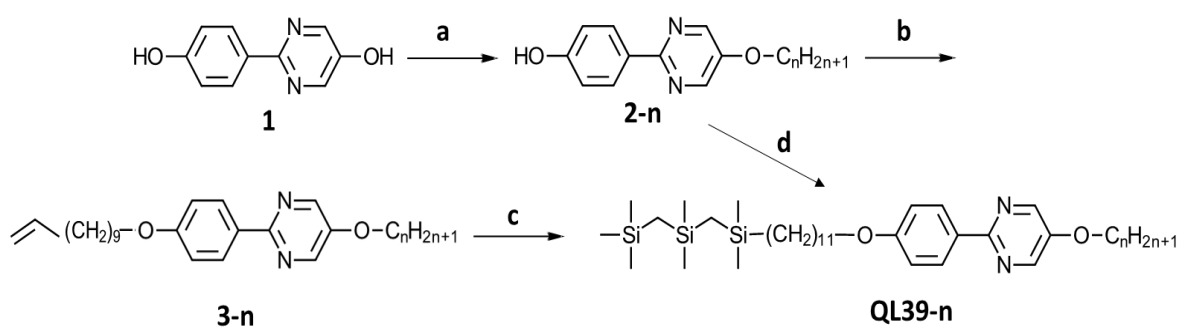
Scheme 2-1 Reagent and conditions: (a) $C_nH_{2n+1}OH$, DIAD,PPh$_3$,THF, rt, overnight or $C_nH_{2n+1}Br$ K$_2$CO$_3$, methyl ethyl ketone, reflux, overnight; (b) C$_{11}$H$_{21}$OH, DIAD, PPh$_3$, THF, rt.overnight; (c) 1,1,1,3,3,5,5-heptamethyltrisilane, Karstedt's catalyst, toluene, 48 h; (d) 1-bromo-12,12,14,14,16,16-hexamethyl-12,14,16-trisilaheptadecane, K$_2$CO$_3$, methyl ethyl ketone.
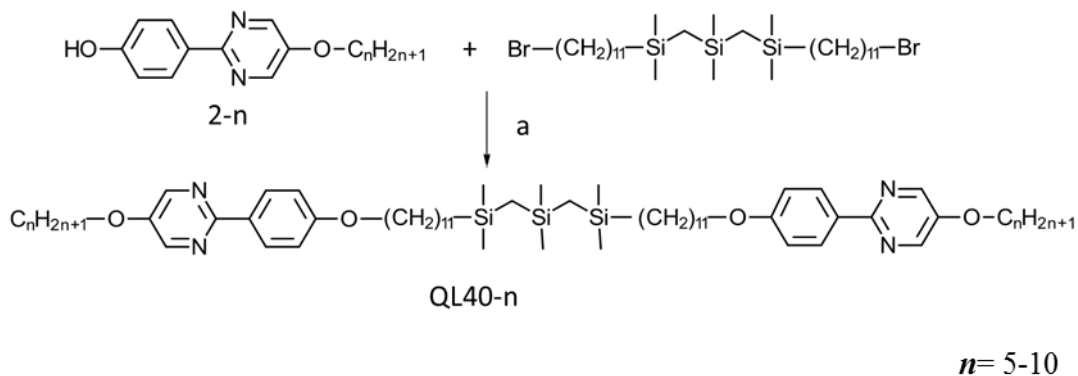
Scheme 2-2 Reagent and conditions: (a) K_2CO_3, methyl ethyl ketone, reflux, overnight.

2.2 Mesophase Characterization

The mesophases formed by the **QL39-*n*** monomers and **QL40-*n*** dimers were characterized using polarized optical microscopy (POM) in Figure 2-1, 2-2 and differential scanning calorimetry (DSC) in Figure 2-3, 2-4. All the **QL39-*n*** monomeric mesogens in the series $n = 5-10$ exhibited only a low-birefringence grey Schlieren texture upon heating and cooling, which is characteristic of the SmC phase (Figure 2-1). On the other hand, the **QL40-*n*** dimers formed a SmA phase on cooling from isotropic liquid, as shown by the characteristic fan textures and dark homeotropic domains (Figure 2-2a). We also observed significant changes in texture at lower temperatures below the SmA phase for **QL40-5**, **QL40-6, QL40-7**, and **QL40-8,** where the dark homeotropic domains transformed to a grey texture. This implies that the phase was tilted, however, no broken fans were observed (Figure 2-2b). Furthermore, this change was accompanied by a change in interference colors, which generally results from a change in the birefringence. Hence, this unidentified phase was denoted as a SmX phase. This change, which was not detected via DSC (Figure 2-4) and for which it was impossible to measure the optical tilt angles (θ_{opt}) using POM, may be due to an unusual layer contraction of the dimer structure. We will see later, through the results of X-ray scattering

experiments and electro-optic response analysis, that this phase does not behave like either the SmC phase, or the SmCa (anticlinic) phase, in which the molecules of two adjacent layers have opposite tilt orientations. Furthermore, the fact that the SmA phase is not observed for the monomeric series suggests that the properties of the dimer and monomer are clearly different.
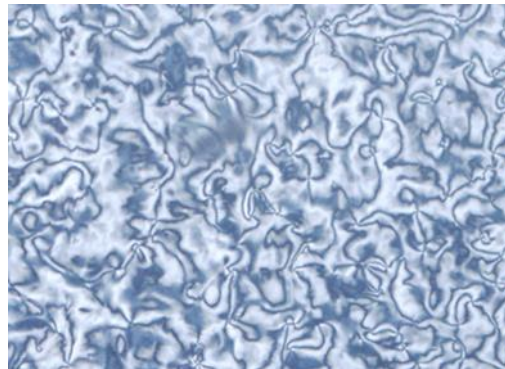
Figure 2-1: Polarized photomicrograph of **QL39-6** monomer on cooling: SmC phase at 70°C.
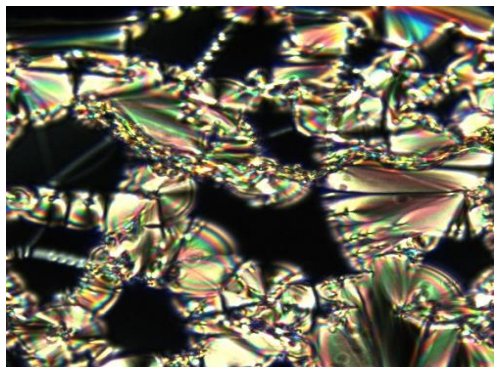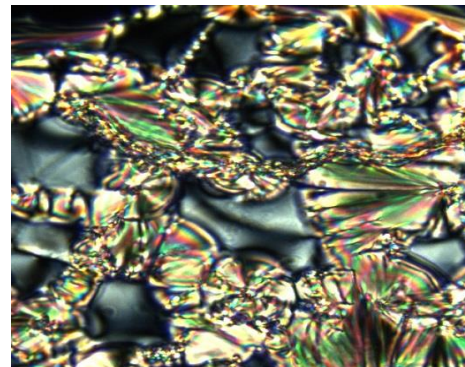
(a)	(b)

Figure 2-2: Polarized photomicrographs of **QL40-6** dimer on cooling: (a) SmA phase at 91 °C and (b) SmX phase at 74 °C.
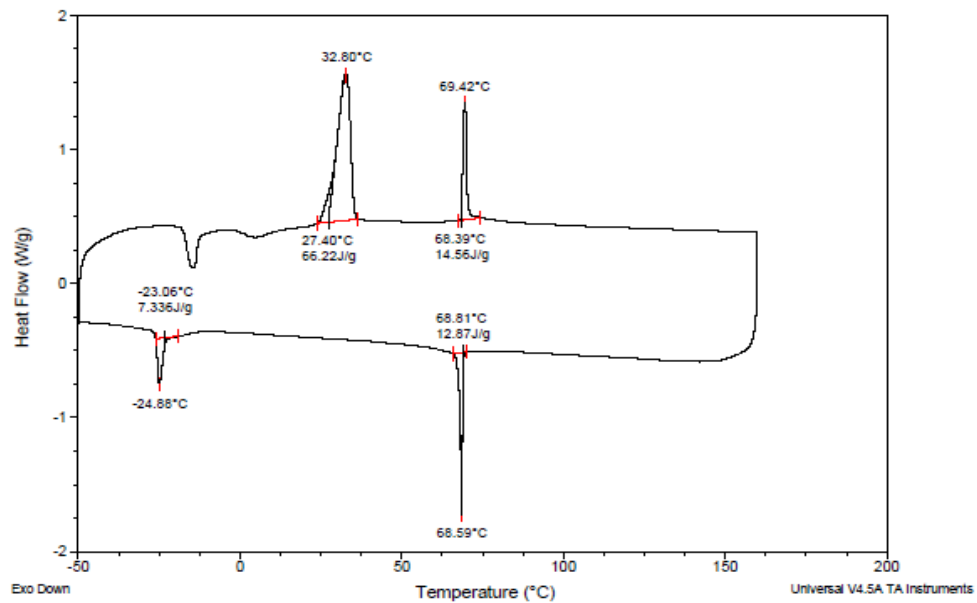
Figure 2-3: DSC profile for **QL39-6** compound taken at 5 K/min scan rate.
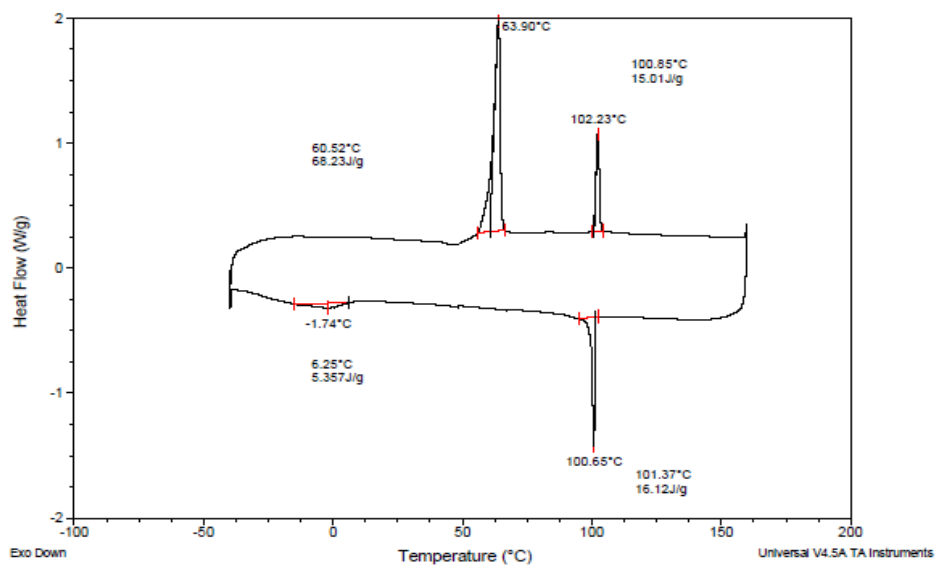
Figure 2-4: DSC profile for **QL40-6** compound taken at 5 K/min scan rate.

28
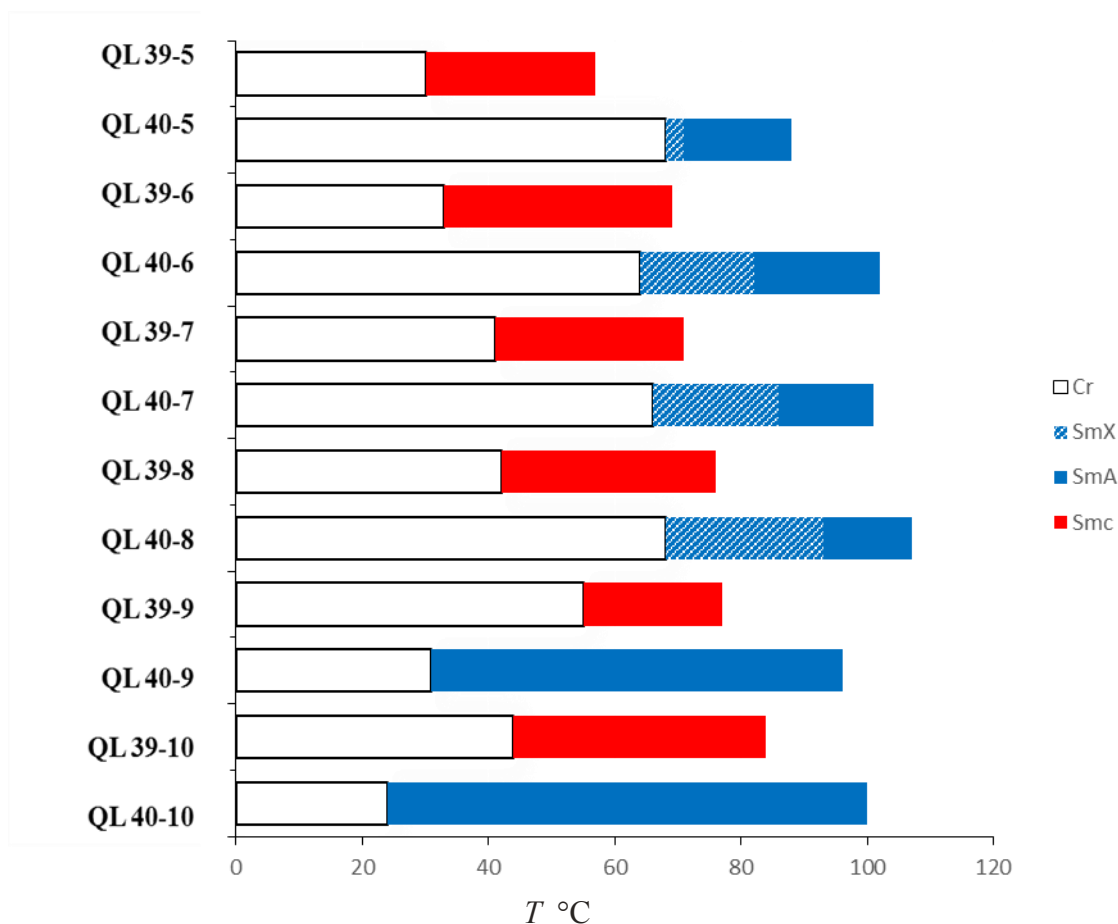
Figure 2-5: Phase transition temperatures °C for **QL39-*n*** monomeric series and **QL40-*n*** dimeric series measured via DSC upon heating at 5 K/min rate.

As shown in Figure 2-5, the temperature ranges of the SmC and SmA phases formed by the **QL39-*n*** and **QL40-*n*** series, respectively, tend to have similar ranges for C_6–C_8, narrower with C_5, and broader with C_{10}. In addition, the SmX range in **QL40-6-8** is similar on average at approximately 21 K. In general, going from the monomer to dimer causes a significant increase in the clearing point (by 27 K on average), which corresponds to an increase in the stability of the smectic layer[1] (the smectic mesophase exists on dimers and monomers at temperatures above room temperature). The difference in the observed clearing points may reflect a difference in the degree of nanosegregation on the momomer and dimer. Furthermore, the dimers **QL40-*n*** exhibit a more significant increase in their melting points (by 30 K on

average) relative to the corresponding monomers, except in the case of the C_9 and C_{10} dimers, for which the melting points decrease by 24 and 20 K, respectively (Figure 2-5). In both series, the enthalpy changes are consistent with first-order transitions from the crystalline-smectic and smectic-isotropic liquid transitions. The transition temperatures and enthalpies of transition measured via DSC for the monomers and dimers are listed in Table 2-1.

Table 2-1 Transition temperatures °C and enthalpies of transition (kJ mol^{-1}, in parentheses) for **QL39- _n_** and **QL40- _n_** compounds.

Compounds	Cr	SmX	SmA	SmC	I
QL 39-5	● 30 (40)			● 57 (7)	●
QL 39-6	● 33 (43)			● 69 (9)	●
QL 39-7	● 41 (49)			● 71 (8)	●
QL 39-8	● 42 (43)			● 77 (10)	●
QL 39-9	● 55 (59)			● 77 (8)	●
QL 39-10	● 44 (41)			● 84 (11)	●
QL 40-5	● 68 (79)	●72	●88 (11)		●
QL 40-6	● 64 (72)	●85	●102 (15)		●
QL 40-7	● 66 (74)	●88	●101 (16)		●
QL 40-8	● 68 (66)	●93	●107 (14)		●
QL 40-9	● 31 (46)		●96 (12)		●
QL 40-10	● 24 (40)		● 100 (19)		●

2.3 X-ray Scattering Experiments

In order to investigate the structure of the smectic phases formed by the dimeric mesogens, small-angle X-ray scattering (SAXS) and monodomain 2D X-ray scattering were performed. The layer spacing d was measured as a function of temperature for the **QL40-6** dimer using SAXS in accordance with Bragg's equation:

$$n\lambda = 2d\sin\theta \qquad (2.1)$$

where n is a positive integer and λ is the wavelength of the incident radiation.

As shown in Figure 2-6, d was measured upon heating from the crystalline phase, and it is more or less invariant of temperature between 84 and 102 °C. It decreased significantly at lower temperatures, with a maximum layer contraction of 9 %. Furthermore, the apparent transition point is identical to that for the SmA-SmX phase transition, for which the dark homeotropic domains transition to a grey texture under POM; this would appear to be consistent with a conventional SmA-SmC transition. The d values obtained from X-ray analysis of the SmA phase (42.5 Å) are smaller than the length of the fully extended **QL40-6** (L= 73.3 Å), calculated according to the model (Figure 2-7). The ratio of $d/L = 0.57$ suggests that the molecules in the SmA phase have a intercalated bilayer arrangement[2]. This arrangement is a typical result of mixing between a terminal chain and spacer in a dimer[2,3]. In addition, the stability of this arrangement depend on the nature of the interaction between the spacer (tricarbosilane) and the end alkyl chains[2].

The 2D X-ray scattering patterns for **QL-40-6** at $T - T_{AX} = +15$ K and $T - T_{AX} = -10$ K are shown in Figure 2-8. Both patterns show the known features of the X-ray diffraction (XRD) patterns of the SmA phase at both 70 and 100 °C. The X-ray patterns exhibit layered structure

characteristics that are observed as a sharp Bragg reflection along the layer normal **z** in the small-angle region; these characteristics correspond to smectic layering.

In addition, a diffuse wide-angle scattering is observed along the axis orthogonal to **z**, which corresponds to the intermolecular distances of the hydrocarbon and carbosilane segments[4]. This analysis via 2D X-ray scattering of a monodomain shows no azimuthal rotation of the wide-angle reflection relative to the small-angle reflection at the apparent SmA-SmX transition point (Figures 2-8). This is clearly shown in Figure 2-9 in which both small and wide angle intensity profiles versus azimuthal angle at 70 °C are compared. This is inconsistent with the observation of behavior such as transformation of the dark homeotropic domains to a grey texture, which, at first, suggests a SmC phase organization.
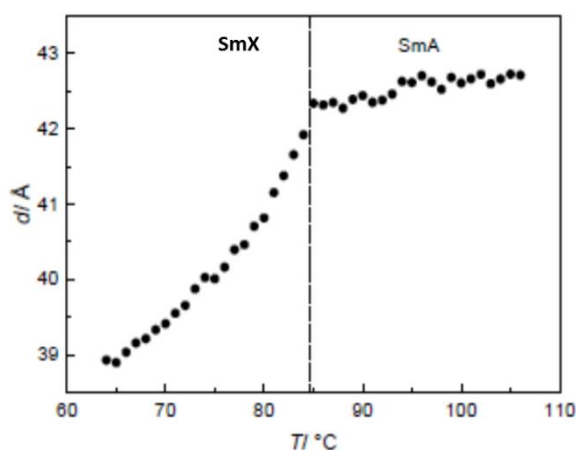
Figure 2-6. Smectic layer spacing d versus reduced temperature $T - T_x$ for **QL40-6** compound.

73.4 Å
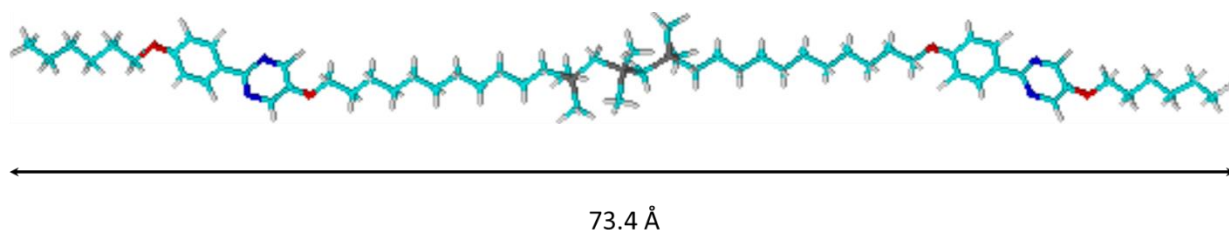
Figure 2-7. Fully extended calculated model of **QL40-6** dimer at 3D Optimization (ACDLABS/3D).
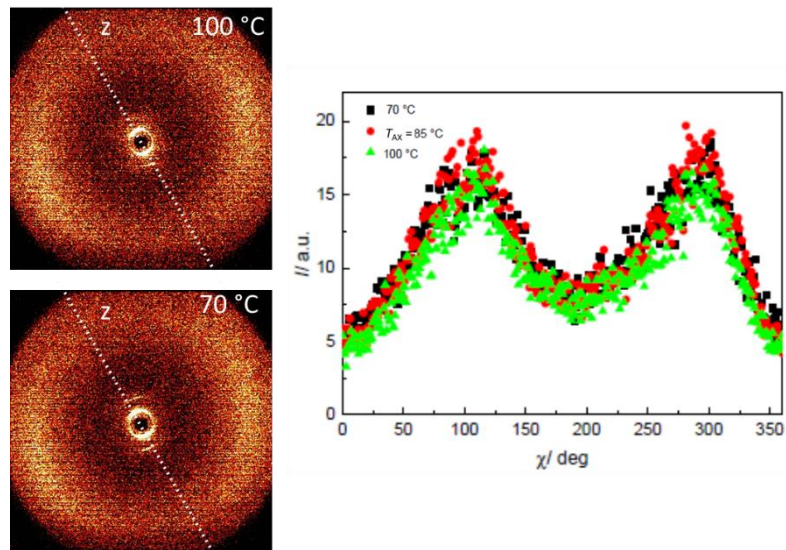
Figure 2-8. 2D X-ray scattering patterns at $T - T_{AX} = +15$ K and $T - T_{AX} = -10$ K (left), and diffuse wide-angle scattering as function of azimuthal angle χ for **QL40-6** at 70, 85 and 100 °C (right).
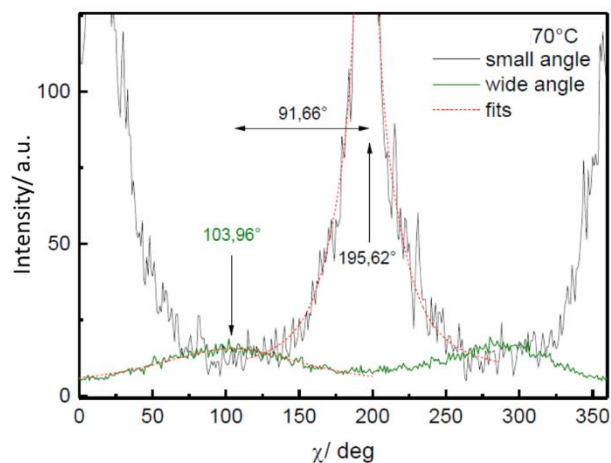
Figure 2-9. χ scan for the wide-angle and small-angle at 70°.

To understand the behavior of the **QL40-6** dimer more fully, we measured the orientational order parameter S_2 from 2-D X-ray scattering measurements of the wide-angle azimuthal intensity profiles $I(\chi)$, which are obtained by integrating the intensity results from the 2D X-ray diffraction patterns. As shown in Figure 2-10, the phase transition from SmA to SmX is not discernible in the S_2 profile; that is, no clear jump is apparent, and it is therefore difficult to assume that the interference color change observed in the texture analysis (the color changed from red to green during the SmA to SmX transition, as shown in Figure 2-2) is consistent with a change in the S_2 values.
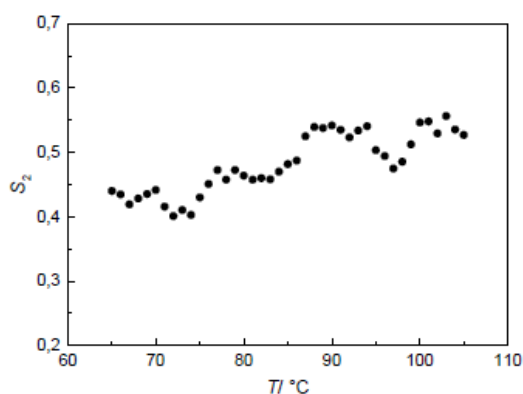
Figure 2-10. Orientational order parameter S_2 vs. temperature for **QL40-6** compound.

2. 4 Electro-Optic Response

In order to confirm that the **QL40-6** dimer does not form a tilted smectic phase or an anticlinic phase, we investigated the electro-optical behavior of the mesophases formed by the monomer **QL39-6** and **QL40-6** upon doping with the chiral dopant **QL32-6** (5 mol%)[5], using POM. The two samples were introduced in commercial indium-tin oxide (ITO) glass slides with a rubbed nylon alignment substrate (4.0-µm spacing). The doped **QL39-6** sample, which forms a SmC* phase only, exhibited good alignment, with contrasting dark and bright texture domains.

Furthermore, application of a triangular wave voltage across the film (6 V/µm, 100 Hz) produced a polarization reversal current response consisting of one polarization peak, which is consistent with a ferroelectric ground state that is consistent with a SmC* phase (Figure 2-11 a). On the other hand, the doped **QL40-6** sample, which was aligned under the same conditions, did not respond to a triangular wave voltage across the film for either the high-temperature SmA* and low-temperature SmX*. This sample did not exhibit any polarization reversal current or any evidence of switching behavior under POM (Figure 2-11b). Hence, both the electro-optical response behavior and the results of the X-ray measurements confirm that the SmX mesophase formed by the **QL40-6** dimer is neither a synclinic SmC phase nor an anticlinic SmC$_a$. Note that the latter would exhibit antiferroelectric behavior upon doping with **QL32-6**, which would show two polarization reversal current peaks instead of one, as shown in Figure 2-12[6].

QL32-6

(a) (b)
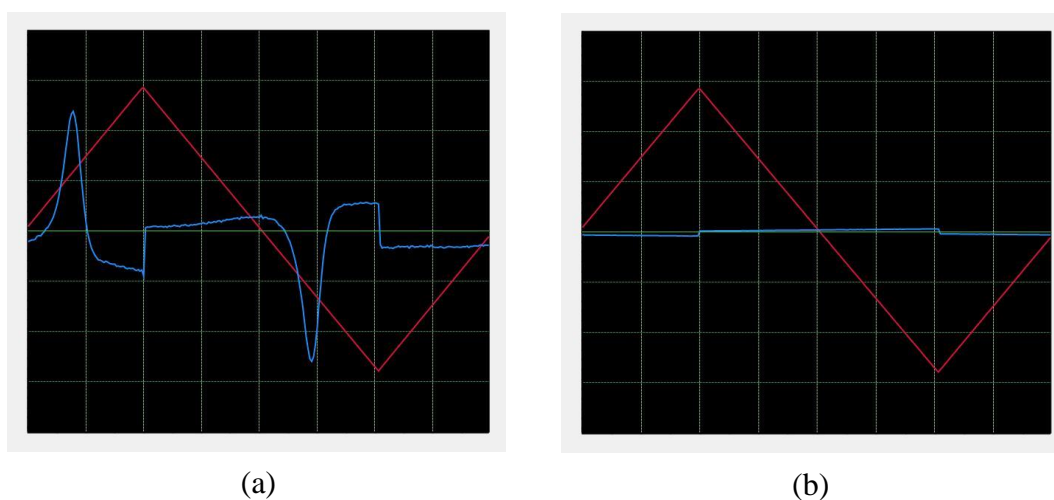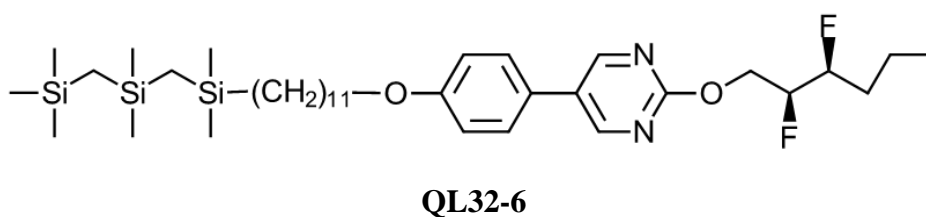
Figure 2-11. Polarization reversal current profiles for surface-stabilized films (4 µm) of (a) **QL39-6** and (b) **QL40-6** (in the SmX phase), both doped with the chiral mesogen **QL32-6** (5 mol%), upon application of triangular AC voltage of 6 V/µm and 100 Hz.
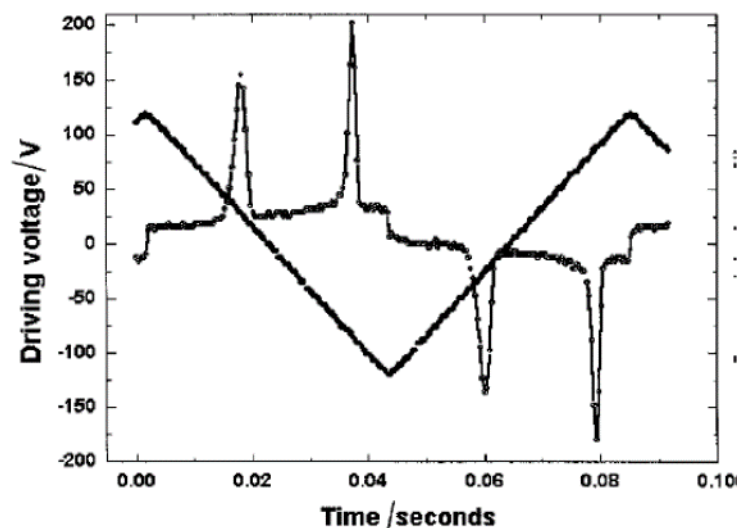
Figure 2-12. Two polarization current peaks appear for smectic C antiferroelectric phase in response to triangular voltage waveform (ref. 6).

2.5 SmX phase

The SmX phase formed by the dimer exhibits unusual and complex behavior that is clearly different from that observed for the corresponding monomer. The SmA phase formed by **QL40-6** (identified via POM) was confirmed by XRD. Further, the SmX phase in the same compound appears to be a SmA phase with an unusual layer contraction. In order to understand the behavior during the change from monomer to dimer, we must obtain a structural model for **QL40-6**. It is important to note that the monomeric molecules are essentially different from the dimeric molecule with respect to the molecular length and the density of the molecular end-groups. From Mulligan[7], we understand the monomer in which the carbosilane end-groups are accommodated in the layers ,and also how the compound having a bilayer intercalated arrangement with nanosegregation produces a significant amount of free volume in the hydrocarbon sub-layer. **QL40-6** also forms a bilayer intercalated arrangement that retains a constant *d* value corresponding to half the molecular length.

Ultimately, the difference between the two models is that the one incorporating the tricarbosilane spacer will not have a spherically shape on the time average like that predicted for the tricarbosilane end-group. This is because the molecules are oriented perpendicular to the layers, with the two mesogenic units extending in opposite directions along **z** (system uniaxiality)[6], which will result in a tricarbosilane spacer with more extended conformations (Figure 2-13). Therefore, a tricarbosilane spacer should have a smaller cross-section on the time-average. We note that a monocarbosilane end-group with a small cross-section has a lower degree of nanosegregation a tricarbosilane end-group, which reduces the degree of SmC-promotion character of the carbosilane unit and may explain why **QL40-*n*** forms an SmA phase instead of an SmC phase. In the case of the SmX phase, *d* contracts with decreasing temperature, which may be a consequence of an increase in core-core interactions that drives an increase in intercalation.
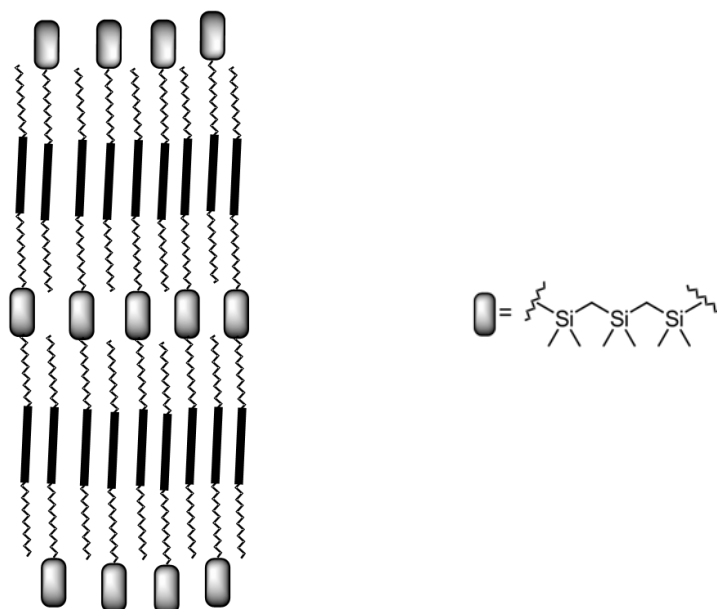
Figure 2- 13. Schematic representation of bulky size of tricarbosilane unit for dimer SmA phase.

2.7 Conclusions

The two new series of carbosilane liquid-crystal dimers and monomers were synthesized with a 2-phenylpyrimidine scaffold and tricarbosilane spacer and end-groups, respectively. The results clearly show that the dimers and monomers have very different mesomorphic properties, which may be related to the difference in flexibility of the tricarbosilane units in a lamellar organization. The monomers (**QL39-n**) form only a tilted SmC phase, whereas the dimers **QL40-n** form an orthogonal SmA phase together with a lower temperature SmX phase. The SmX phase has shown some characteristics of the SmC phase, including a birefringent Schlieren texture and a contraction of the layer spacing, but 2-dimensional X-ray scattering and electro-optical response experiments strongly suggest that the SmX is an orthogonal phase with unusual layer contraction of the dimer structure. Furthermore, the observed increase in clearing point from the monomers to dimers may reflect a difference in the degree of nanosegregation on the monomers and dimers as well as a difference in the strength of van der Waals interactions between the core structures. This would be consistent with our hypothesis that the tricarbosilane spacer in **QL40-*n*** has a smaller cross-section on the time- average compared with the monomer[7]. It remains unclear why the layer spacing in **QL40-*n*** decreases upon SmA-SmX transition, although one might speculate that the layer contraction is due to an increase in the degree of interdigitation.

2.7 Reference

(1) Dunmur, D. *Liquid Crystal Fandmantals*; *Physical Properties of Liquid Crystal*, 2002

(2) Demus, D.; Goodby, J.; Gray, G. W.; Spiess, H. W.; Vill, V. *Handbook of Liquid Crystals, Volume 7: Liquid Crystal Dimers and Oligomers*, 1998.

(3) Imrie, C. T.; Henderson, P. A. *Chem. Soc. Rev.,* **2007**, *36*, 2096.

(4) Schubert, C. P.; Bogner, A.; Porada, J. H.; Ayub, K.; Andrea, T.; Giesselmann, F.; Lemieux, R. P. *J. Mater. Chem. C* **2014**, *2*, 4581.

(5) Schubert, C. P.; Müller, C.; Wand, M. D.; Giesselmann, F.; Lemieux, R. P. *Chem. Commun.*, **2015**, 51.

(6) Robinson, W. K.; Carboni, C.; Kloess, P.; Perkins, S. P.; Coles, H. J. *Liq. Cryst.*, **1998**, *25*, 301.

(7) Mulligan, K. M.; Bogner, A.; Song, Q.; Shubert, P. J.; Giesselmann, F.; Lemieux, R. P. *J. Mater. Chem. C* **2014**, *2*, 8270.

Chapter 3. Experimental

3.1. Syntheses and Characterization

3.1.1. General

^{1}H NMR and ^{13}C NMR spectra were recorded using a Bruker Avance 400 spectrometer; chemical shifts are reported in parts per million (ppm) relative to tetramethylsilane (TMS). Mass spectra were recorded using using a Waters/Micromass GC-TOF (low resolution and high resolution) in electron impact ionization (EI) mode. Differential scanning calorimetry (DSC) analyses were performed on a TA Instruments Q2000 instrument with scanning rate of 5 K min^{-1}. Texture analyses were performed using a Nikon Eclipse E600 POL polarized microscope fitted with a Linkam LTS 350 hot stage and TMS 93 temperature controller. Small-angle X-ray scattering experiments were performed on a SAXSess system from Anton Paar GmbH. Unaligned samples (filled into Hilgenberg Mark capillary tubes of 0.7 mm diameter) were mounted in a temperature controlled sample holder unit (TSC 123). The X-ray beam from a ceramic 107 tube generator was focused by a bent multilayer mirror and shaped by a line collimation block. The X-ray scattering was recorded with a CCD detector (KAF 2084x2083 SCX) and processed and analysed using the SAXSquant 3.5 software.

3.1.2. Materials

All solvents and reagents were obtained from commercial source and used without further purification unless otherwise noted. Anhydrous THF and toluene were obtained from a Solv-

Tek, Inc. solvent purification system. Chemical were obtained from commercial source except for 2,2,4,4,6-pentamethyl-2,4,6-trisilaheptane, which was synthesized by Dr. Kirk Mulligan according to literature procedures[1], and 1,27-dibromo-12,12,14,14,16,16-hexamethyl-12,14 ,16-trisilaheptacosane, which was synthesized by Dr. Christopher Schubert.

3.1.3 Synthesis of QL39-n Liquid Crystal Monomers
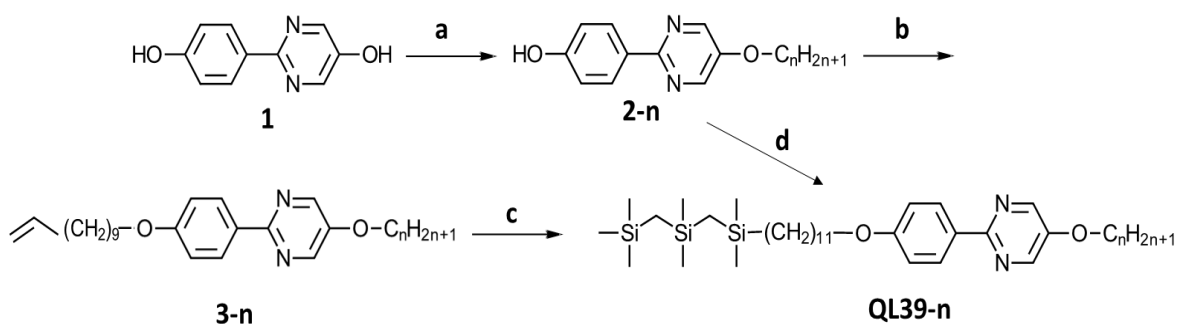
Reagent and conditions: (a) $C_nH_{2n+1}OH$, DIAD,PPh₃,THF, rt, overnight or $C_nH_{2n+1}Br$ K₂CO₃, methyl ethyl ketone, reflux, overnight; (b) $C_{11}H_{21}OH$, DIAD, PPh₃, THF, rt.overnight; (c) 1,1,1,3,3,5,5-heptamethyltrisilane, Karstedt's catalyst, toluene, 48 h; (d) 1-bromo-12,12,14,14,16,16-hexamethyl-12,14,16-trisilaheptadecane, K₂CO₃, methyl ethyl ketone.

4-(5-Pentyloxypyrimidin-2-yl)phenol (2-5). To a mixture of 2-(4-hydroxyphenyl)pyrimidin -5-ol (**1**, 2.0 g, 10.6 mmol), pentan-1-ol (9.34 g, 10.6 mmol) and Triphenylphosphine (PPh₃) (5.24 g, 20.2 mmol) in dry Tetrahydrofuran (THF) (100 mL) was added dropwise Diisopropyl azodicarboxylate (DIAD) (4.04 g, 20.2 mmol) at room temperature. After stirring for 24 h, the solvent was removed under reduced pressure and the solid residue was purified by column chromatography on silica gel (3:1 hexane/EtOAc) to give **2-5** as a beige solid (1.5 g, 55%): ^{1}H NMR (400 MHz, CDCl₃) δ (ppm) 8.44 (s, 2 H), 8.27 (d, J = 9.1 Hz, 2 H), 6.95 (d, J = 8.8 Hz, 2 H), 5.15 (s, 1 H), 4.09 (t, J = 6.4 Hz, 2 H), 1.84 (m, 2 H), 1.53-1.42 (m, 4 H), 0.96 (t, J = 6.6 Hz, 3 H): ^{13}C NMR (100 MHz, CDCl₃) δ 160.1, 157.7, 151.2, 143.9, 131.3, 129.4, 115.6, 69.1,

28.7, 28.0, 22.4, 14.0; LRMS (EI) *m/z* 258 ([M]$^+$,48), 189 (17), 188 (100),159 (12), 132 (20), 119 (34), 105 (18) ; HRMS (EI) m/z calcd for C$_{15}$H$_{18}$N$_2$O$_2$ 258.1368, found 258.1361.

4-(5-Hexyloxypyrimidin-2-yl)phenol (2-6). The procedure described for the synthesis of **2-5** was repeated with hexan-1-ol (1.08 g, 10.6 mmol) and 2-(4-hydroxyphenyl)pyrimidin -5-ol (2.0 g, 10.6 mmol) to give **2-6** as a beige solid (1.46 g, 50%): ^{1}H NMR (400 MHz, CDCl$_3$) δ (ppm) 8.43 (s, 2 H), 8.20 (d, *J* = 9.1 Hz, 2 H), 6.83 (d, *J* = 8.8 Hz, 2 H), 5.21 (s, 1 H), 4.09 (t, J = 6.4 Hz, 2 H), 1.92-1.75 (m, 2 H), 1.53-1.42 (m, 2 H), 1.36 (dq, J = 7.2, 3.6 Hz, 4 H), 0.98 (t, J = 6.6 Hz, 3 H): ^{13}C NMR (100 MHz, CDCl$_3$) δ 160.1, 157.5, 151.2, 143.9, 130.0, 129.3, 115.5, 69.0, 31.5, 29.0, 25.5, 22.4, 14.0. LRMS (EI) *m/z* 272 (M+, 55), 189 (14), 188 (100), 159 (6), 132 (8), 105 (4); HRMS (EI) m/z calcd for C$_{16}$H$_{20}$N$_2$O$_2$ 272.1525, found 272.1519.

4-(5-Heptyloxypyrimidin-2-yl)phenol (2-7). The procedure described for the synthesis of **2-5** was repeated with heptan-1-ol (1.23 g, 10.6 mmol) and 2-(4-hydroxyphenyl)pyrimidin -5-ol (2.0 g, 10.6 mmol) to give **2-7** as a beige solid (1.8 g, 59%): ^{1}H NMR (400 MHz, CDCl$_3$) δ (ppm) 8.42 (s, 2 H), 8.25 (d, *J* = 8.8 Hz, 2 H), 6.92 (d, *J* = 8.8 Hz, 2 H), 4.97 (s, 1 H), 4.09 (t, J = 6.4 Hz, 2 H), 1.86-1.82 (m, 2 H), 1.53-1.42 (m, 2 H), 1.42-138 (m, 6 H), 0.91 (t, J = 6.9 Hz, 3 H): ^{13}C NMR (100 MHz, CDCl$_3$) δ 169.1, 157.5, 152.0, 143.5, 132.4, 129.1, 115.8, 68.0, 32.5, 29.3, 28.95, 25.5, 23.6, 14.0. LRMS (EI) *m/z* 286 (M+, 90), 202 (38), 189 (32), 188 (100), 159 (5), 57 (21); HRMS (EI) *m/z* calcd for C$_{17}$H$_{22}$N$_2$O$_2$ 286.1681, found 286.1666.

4-(5- Octyloxypyrimidin-2-yl)phenol (2-8). The procedure described for the synthesis of **2-5** was repeated with octan-1-ol (1.30 g, 10.6 mmol) and 2-(4-hydroxyphenyl)pyrimidin -5-ol (2.0 g, 10.6 mmol) to give **2-8** as a beige solid (1.40 g, 46%): ^{1}H NMR (400 MHz, CDCl3) δ (ppm) 8.43 (s, 2 H), 8.91 (d, *J* = 8.8 Hz, 2 H), 6.97 (d, *J* = 8.8 Hz, 2 H), 5.45 (s, 1 H), 4.09 (t, J = 6.4 Hz, 2 H), 1.85-1.82 (m, 2 H), 1.52-1.42 (m, 2 H), 1.42-138 (m, 6 H), 0.92 (t, J = 6.6 Hz, 3 H): ^{13}C NMR (100 MHz, CDCl$_3$) δ 160.1, 157.0, 151.0, 143.5, 131.3, 129.0, 115.2, 68.7, 31.5, 28.94, 28.85, 28.77, 25.5, 22.5, 13.7. LRMS (EI) *m/z* 300 (M+, 44), 189 (14), 188 (100), 159

(5), 132 (6), 119 (11), 105 (50); HRMS (EI) *m/z* calcd for $C_{18}H_{24}N_2O_2$ 300.1831, found 300.1838.

4-(5- Nonyloxypyrimidin-2-yl)phenol (2-9). A mixture of 2-(4-hydroxyphenyl)pyrimidin-5-ol (2.0 g, 10.6 mmol), K_2CO_3 (4.39 g, 31.8 mmol) and 1-bromononane (2.20 g, 10.6 mmol) in acetone (80 mL) was heated to reflux for 24 h. After cooling, the solvent was removed under reduced pressure, and the solid residue was dissolved in DCM (60 mL) and washed with dilute HCl (1 M, 20 mL), brine (60 mL), dried ($MgSO_4$) and concentrated. The crude product was purified by flash chromatography on silica gel (3:1 hexane/EtOAc) to give **2-9** as a beige solid (1.65 g, 50%): ^{1}H NMR (400 MHz, $CDCl_3$) δ (ppm) 8.42 (s, 2 H), 8.91 (d, J = 8.8, 2 H), 6.97 (d, J = 8.8 Hz, 2 H), 4.94 (s, 1 H), 4.09 (t, J = 6.4 Hz, 2 H), 1.85-1.82 (m, 2 H), 1.52-1.42 (m, 2 H), 1.42-1.38 (m, 8 H), 0.92 (t, J = 6.8 Hz, 3 H): ^{13}C NMR (100 MHz, $CDCl_3$) δ 160.1, 157.3, 153.8, 144.1, 136.0, 129. 6, 115.7, 68.8, 31.5, 29.7, 29.6, 29.2, 28.9, 25.9, 22.5, 14.4; LRMS (EI) *m/z* 314 (M+, 100), 189 (8), 188 (62), 57 (1); HRMS (EI) *m/z* calcd for $C_{19}H_{26}N_2O_2$ 314.1989, found 314.1994.

4-(5- Decyloxypyrimidin-2-yl)phenol (2-10). The procedure described for the synthesis of **2-9** was repeated with 1-bromodecane (2.35 g, 10.6 mmol) and 2-(4-hydroxyphenyl) pyrimidin -5-ol (2.0 g, 10.6 mmol) to give **2-10** as a beige solid (1.8 g, 51%): ^{1}H NMR (400 MHz, $CDCl_3$) δ (ppm) 8.42 (s, 2 H), 8.91 (d, J = 8.8 Hz, 2 H), 6.97 (d, J = 8.8 Hz, 2 H), 4.94 (s, 1 H), 4.98 (t, J = 6.4 Hz, 2 H), 1.85-1.82 (m, 2 H), 1.51-1.42 (m, 2 H), 1.42-138 (m, 10 H), 0.92 (t, J = 6.8 Hz, 3 H): ^{13}C NMR (100 MHz, $CDCl_3$) δ 160.8, 158.3, 152.9, 143.8, 137.0, 129. 4, 115.3, 68.9, 31.8, 30.50, 29.72, 29.60, 28.96, 28.95, 25.8, 22.6, 13.6. LRMS (EI) *m/z* 328 (M+, 100), 189 (10), 188 (85), 57 (2); HRMS (EI) *m/z* calcd for $C_{20}H_{28}N_2O_2$ 328.2159, found 328.2159.

5-Hexyloxy-2-(4-(undec-10-enyloxy)phenyl)pyrimidine (3-6). The procedure described for the synthesis of **2-5** was repeated with **2-6** (1.46 g, 5.3 mmol) and 10-undecen-1-ol (0.90 g,

5.3 mmol), to give **3-6** as a yellow solid (0.93 g, 41%): ^{1}H NMR (400 MHz, CDCl$_3$) δ (ppm)

8.42 (s, 2 H), 8.28 (d, J = 8.84 Hz, 2 H), 6.98 (d, J = 8.84 Hz, 2 H), 5.82 (ddt, J = 17.05, 10.29,

6.66, 6.66 Hz, 1 H), 5.09 - 4.87 (dd, 2 H), 4.17 - 3.94 (two separate triplets m, 4 H), 2.05 (q, J

= 6.82 Hz, 2 H), 1.91 - 1.72 (m, 4 H), 1.55 - 1.25 (m, 18 H), 0.98 - 0.88 (t, 3 H). ^{13}C NMR (100

MHz, CDCl$_3$) δ 157.6, 151.0, 143.3, 139.2, 130.0, 128.9, 114.42, 114.10, 68.94, 68.06, 33.7,

31.49, 29.50, 29.37- 29.11 (several overlapping peaks), 28.9, 26.0, 25.5, 22.5, 14.0 LRMS (EI)

m/z 424 ([M]$^+$, 17), 303 (4), 272(15), 188 (100),107 (4), 81 (13), 67(18) ; HRMS (EI) *m/z* calcd

for C$_{27}$H$_{40}$N$_2$O$_2$ 424.3079, found 424.3090.

5-Pentyloxy-2-[4-(12,12,14,14,16,16-hexamethyl-12,14,16-trisilaheptadecyloxy)phenyl]

pyrimidine (**QL39-5**). A mixture of **2-5** (0.23 g, 0.885 mmol), K$_2$CO$_3$ (0.85 g, 6.16 mmol)

and 1-bromo-12,12,14,14,16,16-hexamethyl-12,14,16-trisilaheptadecane (0.20 g, 0.442 mmol)

in acetone (40 mL) was heated to reflux for 24 h. After cooling, the solvent was removed under

reduced pressure, and the solid residue was dissolved in DCM (20 mL) and washed with dilute

HCl (1M, 20 mL), brine (20 mL), dried (Mg$_2$SO$_4$) and concentrated. The crude product was

purified by flash chromatography on silica gel (3:1 hexane/EtOAc) to give **QL39-5** as a white

sold (0.23 g, 83%) Recrystallization from ethanol :^{1}H NMR (400 MHz, CDCl$_3$) δ (ppm) 8.45

(s, 2 H), 8.31 (d, *J* = 8.8 Hz, 2 H), 6.99 (d, *J* = 8.81 Hz, 2 H), 4.11 - 4.03 (these are two separate

triplets dt, 4 H), 1.87 - 1.81 (m, 4 H), 1.50 - 1.25 (m, 20 H), 0.97 (t, *J* = 7.05 Hz, 3 H),), 0.49

(br t, 2 H), 0.05 (s,6 H), 0.03 (s, 9 H), 0.00 (s, 6 H), -0.25 (s, 2 H), -0.28 (s, 2 H); ^{13}C NMR

(100 MHz, CDCl$_3$) δ 161.53, 161.05, 151.7, 147.8, 132.3, 129.4, 114.6, 69.2, 68.1, 34.0, 29.57,

29.41-28.72 (several overlapping peaks), 28.0, 26.0, 24.0, 22.3, 18.0, 14.0, 5.7, 4.0, 2.4, 1.5, -

0.4. LRMS (EI) *m/z* 628 ([M]$^+$, 100), 629, 614(14), 613(25), 412(10), 217 (15), 129 (10);

HRMS (EI) *m/z* calcd for C$_{35}$H$_{64}$N$_2$O$_2$Si$_3$ 628.427, found 628.428.

Anal. Calcd for C$_{35}$H$_{64}$N$_2$O$_2$Si$_3$: C, 66.85; H, 10.26; N, 4.45; Found: C, 66.74; H, 10.43; N, 4.26.

5-Hexyloxy-2-[4-(12,12,14,14,16,16-hexamethyl-12,14,16-trisilaheptadecyloxy)phenyl] pyrimidine (**QL39-6**). To a solution of **3-6** (0.3 g, 0.70 mmol) and 1,1,1,3,3,5,5-heptamethyltrisilane (0.35 g, 1.415 mmol) in dry toluene (25 mL) was added dropwise Karstedt's catalyst (0.035 ml, 0.035 mmol) at 0 ^{o}C. The mixture was allowed to warm to room temperature and stirred for 48 h. The solvent was removed under reduced pressure and   the crude product was purified by silica gel column chromatography (hexane/ethyl acetate 9:1) to give **QL39-6** (0.37 g, 82%) as a white solid recrystallization from ethanol: ^{1}H NMR (400 MHz, CDCl$_3$) δ (ppm) 8.42 (s, 2 H), 8.28 (d, J = 9.0 Hz, 2 H), 6.98 (d, J = 8.8 Hz, 2 H), 4.15- 3.92 (these are two separate triplets dt, 4 H), 1.91 - 1.72 (m, 4 H), 1.50 - 1.22 (m, 22 H), 0.92 (t, J = 7.0 Hz, 3 H), 0.47 (br t, 2 H), 0.05 (s,6 H), 0.03 (s, 9 H), 0.00 (s, 6 H), -0.25 (s, 2 H), -0.28 (s, 2 H); ^{13}C NMR (100 MHz, CDCl$_3$) δ 160.8, 157.6, 151.0, 143.8, 130.0, 128.9, 114.4, 68.9, 68.0, 33.7, 31.4,29.2-28.96 (several overlapping peaks),28.76,25.5, 22.5, 18.0, 14.0, 5.7, 4.0, 2.4, 1.4, -0.4. LRMS (EI) m/z 642 ([M]$^+$, 100), 627 (24), 501(4), 473(6), 425 (6), 129 (3); HRMS (EI) m/z calcd for C$_{36}$H$_{66}$N$_2$O$_2$Si$_3$ 642.442, found 642.443.

Anal. Calcd for C$_{36}$H$_{66}$N$_2$O$_2$Si$_3$: C, 67.23; H, 10.34; N, 4.36; Found: C, 66.80; H, 10.23; N, 4.33.

5-Heptyloxy-2-[4-(12,12,14,14,16,16-hexamethyl-12,14,16-trisilaheptadecyloxy)phenyl] pyrimidine (**QL39-7).** The procedure described for the synthesis of **QL39-5** was repeated with **2-7** (0.14 g, 0.490 mmol) and 1-bromo-12,12,14,14,16,16-hexamethyl-12,14,16-trisilaheptadecane (0.15 g, 0.332 mmol) to give **QL39-7**   as a white solid (0.18 g, 82%) rerystallization from ethanol ^{1}H NMR (400 MHz, CDCl$_3$) δ (ppm) 8.42 (s, 2 H), 8.29 (d, J = 8.8 Hz, 2 H), 6.99 (d, J = 8.8 Hz, 2 H), 4.10 - 4.01 (these are two separate triplets dt, 4 H), 1.87

- 1.80 (m, 4 H), 1.50 - 1.22 (m, 24 H), 0.93 (t, J = 6.9 Hz, 3 H), 0.48 (br t, 2 H), 0.05 (s, 6 H), 0.03 (s, 9 H), 0.00 (s, 6 H), -0.25 (s, 2 H), -0.28 (s, 2 H); ^{13}C NMR (100 MHz, CDCl$_3$) δ 161.1, 157.4, 153.9, 143.8, 132.3, 128.9, 114.4, 69.4, 68.9, 34.0, 31.7, 29.5- 28.9 (several overlapping peaks), 25.8, 24.0, 22.6, 18.4, 14.0, 6.0, 4.1, 2.4, 1.4, -0.4. LRMS (EI) m/z 657 ([M]$^+$, 100), 641 (53), 625 (4), 569(10), 487(14), 431(14), 415 (5); HRMS (EI) *m/z* calcd for C$_{37}$H$_{68}$N$_2$O$_2$Si$_3$ 657.466, found 657.4698.

Anal. Calcd for C$_{37}$H$_{68}$N$_2$O$_2$Si$_3$: C, 67.66; H, 10.43; N, 4.26; Found: C, 67.71; H, 10.61; N, 4.31.

5-Octyloxy-2-[4-(12,12,14,14,16,16-hexamethyl-12,14,16-trisilaheptadecyloxy)phenyl] pyrimidine (**QL39-8**). The procedure described for the synthesis of **QL39-5** was repeated with **2-8** (0.15 g, 0.510 mmol) and 1-bromo-12,12,14,14,16,16-hexamethyl-12,14,16-trisilaheptadecane (0.19 g, 0.432 mmol) to give **QL39-8** as a white solid (0.23 g, 82%) recrystallization from ethanol: ^{1}H NMR (400 MHz, CDCl$_3$) δ (ppm) 8.43 (s, 2 H), 8.28 (d, J = 8.8 Hz, 2 H), 6.98 (d, J = 8.8 Hz, 2 H), 4.06 (these are two separate triplets dt, 4 H), 1.88 - 1.72 (m, 4 H), 1.50 - 1.22 (m, 26 H), 0.92 (t, J = 7.0 Hz, 3 H),), 0.47 (t, 2 H), 0.05 (s, 6 H), 0.03 (s, 9 H), 0.00 (s, 6 H), -0.25 (s, 2 H), -0.28 (s, 2 H); ^{13}C NMR (100 MHz, CDCl$_3$) δ 160.0, 158.5, 151.1, 147.3, 137.9, 129.1, 114.5, 69.6, 69.0, 33.7, 31.7, 30.0, 29.57, 29.26-28.0 (several overlapping peaks), 25.7, 23.9, 22.5, 18.0, 12.8, 5.8, 4.0, 2.4, 1.4, -0.4 LRMS (EI) *m/z* 670 ([M]$^+$, 100), 453 (22), 217(44), 188(49), 145 (20), 129 (71); HRMS (EI) *m/z* calcd for C$_{38}$H$_{70}$N$_2$O$_2$Si$_3$ 670.4751, found 670.4745.

Anal. Calcd for C$_{38}$H$_{70}$N$_2$O$_2$Si$_3$: C, 68.03; H, 10.52; N, 4.17; Found: C, 67.80; H, 10.15; N, 4.05.

5-Nonyloxy-2-[4-(12,12,14,14,16,16-hexamethyl-12,14,16-trisilaheptadecyloxy)phenyl] pyrimidine (**QL39-9**). The procedure described for the synthesis of **QL39-5** was repeated with

2-9 (0.2 g, 0.664 mmol) and 1-bromo-12,12,14,14,16,16-hexamethyl-12,14,16-trisilaheptadecane (0.2 g, 0.443 mmol) to give **QL39-9** as a white solid (0.27 g, 90%) recrystallization from ethanol: ^{1}H NMR (400 MHz, CDCl$_3$) δ (ppm) 8.42 (s, 2 H), 8.29 (d, J = 8.8 Hz, 2 H), 6.99 (d, J = 8.8 Hz, 2 H), 4.10 (these are two separate triplets dt, 4 H), 1.87 - 1.80 (m, 4 H), 1.48 - 1.29 (m, 28 H), 0.91 (t, J = 7.0 Hz, 3 H),), 0.48 (t, 2 H), 0.05 (s, 6 H), 0.03 (s, 9 H), 0.00 (s, 6 H), -0.25 (s, 2 H), -0.28 (s, 2 H); ^{13}C NMR (100 MHz, CDCl$_3$) δ 162.9, 157.6, 150.5, 143.8, 133.2, 128.9, 114.4, 68.64, 68.09, 33.7, 31.8, 29.4-28.1 (several overlapping peaks), 25.8, 23.9, 22.6, 18.0, 13.8, 5.5, 4.0, 2.4, 1.4, -0.4 LRMS (EI) m/z 684 ([M]$^+$, 100), 640 (21), 386(6), 327(7), 145 (7); HRMS (EI) m/z calcd for C$_{39}$H$_{72}$N$_2$O$_2$Si$_3$ 684.4909, found 684.4902.

Anal. Calcd for C$_{39}$H$_{72}$N$_2$O$_2$Si$_3$: C, 68.39; H, 10.59; N, 4.09; Found: C, 68.09; H, 10.75; N, 4.15.

5-Decyloxy-2-[4-(12,12,14,14,16,16-hexamethyl-12,14,16-trisilaheptadecyloxy)phenyl] pyrimidine (QL39-10). The procedure described for the synthesis of **QL39-5** was repeated with **2-10** (0.15 g, 0.456 mmol) and 1-bromo-12,12,14,14,16,16-hexamethyl-12,14,16-trisilaheptadecane (0.137 g, 0.304 mmol) to give **QL39-10** as a white solid (0.17 g, 80%) recrystallization from ethanol: ^{1}H NMR (400 MHz CDCl$_3$) δ (ppm) 8.42 (s, 2 H), 8.29 (d, J = 8.8 Hz, 2 H), 6.99 (d, J = 8.8 Hz, 2 H), 4.10 (these are two separate triplets dt, 4 H), 1.87 - 1.80 (m, 4 H), 1.48 - 1.29 (m, 30 H), 0.91 (t, J = 6.8 Hz, 3 H),), 0.48 (t, 2 H), 0.05 (s, 6 H), 0.03 (s, 9 H), 0.00 (s, 6 H), -0.25 (s, 2 H), -0.28 (s, 2 H); ^{13}C NMR (100 MHz, CDCl$_3$) δ 161.5, 159.7, 151.1, 147.3, 132.3, 129.1, 114.5, 69.6, 69.0, 33.7, 31.7, 30.0, 29.57, 29.26-28.0 (several overlapping peaks), 27.7, 23.9, 22.5, 18.0, 12.8, 5.8, 4.0, 2.4, 1.4, -0.4 LRMS (EI) m/z 698 ([M]$^+$, 100), 683 (22), 481(14), 188(15), 129 (18); HRMS (EI) m/z calcd for C$_{40}$H$_{74}$N$_2$O$_2$Si$_3$ 698.5058, found 698.5056.

Anal. Calcd for $C_{40}H_{74}N_2O_2Si_3$: C, 68.74; H, 10.67; N, 4.01; Found: C, 69.06; H, 10.70; N, 4.29.

3.1.4 Synthesis of QL40-n Liquid Crystal Dimers
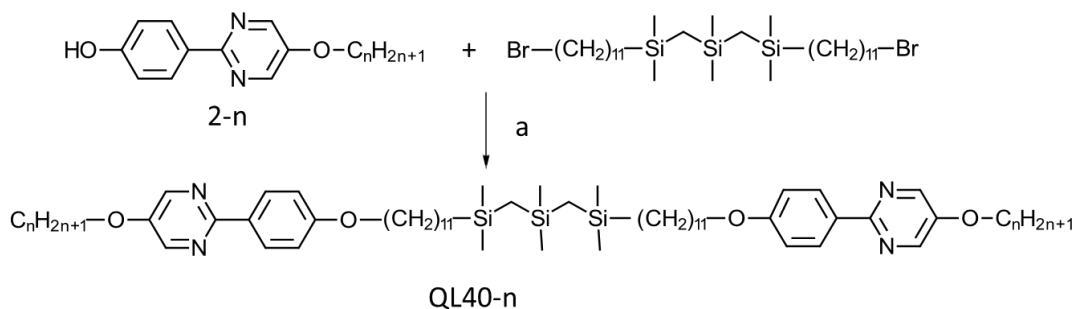
Scheme1 Reagent and conditions: (a) K_2CO_3, methyl ethyl ketone, reflux, overnight.

1,27-Bis-[4-(5-pentyloxypyrimidin-2-yl)phenoxy]-12,12,14,14,16,16-hexamethyl-12,14,16-trisilaheptacosane (QL40-5). A mixture of **2-5** (0.5 g, 1.93 mmol), K2CO3 (0.98 g, 7.09 mmol) and 1,27-dibromo-12,12,14,14,16,16-hexamethyl-12,14,16-trisilaheptacosane (0.432 g, 0.645 mmol) in methyl ethyl ketone (40 mL) was heated to reflux for 24 h. After cooling, the solvent was removed under reduced pressure, and the solid residue was dissolved in DCM (20 mL) and washed with dilute HCl (1 M, 20 mL), brine (20 mL), dried (MgSO4) and concentrated. The crude product was purified by flash chromatography on silica gel (3:1 hexane/EtOAc) to give **QL40-5** as a white solid (0.47 g, 71%) recrystallization from ethanol ^{1}H NMR (400 MHz, CDCl$_3$) δ (ppm) 8.44 (s, 4 H), 8.28 (d, J = 8.8 Hz, 4 H), 6.99 (d, J = 8.8 Hz, 4 H), 4.11 - 4.01 (these are two separate triplets dt, 8 H), 1.86 - 1.79 (m, 8 H), 1.51 - 1.22 (m, 40 H), 0.94 (t, J = 7.0 Hz, 6 H),), 0.47 (t, 4 H), 0.05 (s, 6 H), 0.00 (s, 12 H), -0.28 (s, 4 H); ^{13}C NMR (100 MHz, CDCl$_3$) δ 161.65, 161.05, 151.2, 146.2, 132.3, 129.0, 114.4, 69.2, 68.4, 34.6, 29.91, 29.73-29.12 (several overlapping peaks), 28.0, 25.0, 24.0, 22.3, 18.0, 14.0,

4.0, 2.5, -0.4 LRMS (ESI) *m/z* 1025 ([M+1]$^+$,18),), 1009 (100), 955 (26), 939 (13),767 (27), 751 (37), 735 (23), 597 (38) 541 (21), 525 (12); (HRMS (EIS) *m/z* calcd for $C_{60}H_{100}N_4O_4Si_3$ 1025.71415, found 1025.71251.

Anal. Calcd for $C_{60}H_{100}N_4O_4Si_3$: C, 70.21; H, 9.92; N, 5.46; Found: C, 69.96; H, 9.81; N, 5.43.

1,27-Bis-[4-(5-hexyloxypyrimidin-2-yl)phenoxy]-12,12,14,14,16,16-hexamethyl-12,14,16-trisilaheptacosane (QL40-6). The procedure described for the synthesis of **QL40-5** was repeated with **2-6** (0.25 g, 0.98 mmol) and 1,27-dibromo-12,12,14,14,16,16-hexamethyl-12,14,16-trisilaheptacosane (0.2 g, 0.30 mmol). The crude product was purified by flash chromatography on silica gel (3:1 hexane/EtOAc) to give **QL40-6** as a white solid (0.20 g, 51%) recrystallization from ethanol: ^{1}H NMR (400 MHz, CDCl$_3$) δ (ppm) 8.42 (s, 4 H), 8.28 (d, *J* = 9.0 Hz, 4 H), 6.98 (d, *J* = 8.8 Hz, 4 H), 4.15 - 3.92 (these are two separate triplets dt, 8 H), 1.85 - 1.81 (m, 8 H), 1.51 - 1.22 (m, 44 H), 0.92 (t, *J* = 7.0 Hz, 6 H),), 0.47 (t, 4 H), 0.05 (s, 6 H), 0.00 (s, 12 H), -0.28 (s, 4 H); ^{13}C NMR (100 MHz, CDCl$_3$) δ 160.7, 157.0, 151.0, 143.8, 129.9, 128.9, 114.4, 68.95, 68.09, 33.7, 31.4, 29.62-28.95 (several overlapping peaks), 28.7, 26.0, 25.5, 23.9, 22.5, 18.0, 13.9, 4.1, 2.5, -0.4. LRMS (ESI) *m/z* 1053 ([M+1]$^+$, 100), 1038 (30), 1037 (100), 696 (23), 781 (23) ,765 (33), 611 (32) HRMS (EIS) *m/z* calcd for $C_{62}H_{104}N_4O_4Si_3$ 1053.7438, found 1053.7426.

Anal. Calcd for $C_{62}H_{105}N_4O_4Si_3$: C, 70.69; H, 5.39; N, 9.95; Found: C, 70.19 H, 5.27; N, 9.869.

1,27-Bis-[4-(5-heptyloxypyrimidin-2-yl)phenoxy]-12,12,14,14,16,16-hexamethyl-12,14,16-trisilaheptacosane (QL40-7). The procedure described for the synthesis of **QL40-7** was repeated with **2-7** (0.25 g, 0.894 mmol) and 1,27-dibromo-12,12,14,14,16,16-hexamethyl-12,14,16-trisilaheptacosane (0.2 g, 0.29 mmol) The crude product was purified by flash chromatography on silica gel (3:1 hexane/EtOAc) to give **QL40-7** as a white solid (0.29 g, 90%) recrystallization from ethanol: ^{1}H NMR (400 MHz, CDCl$_3$) δ (ppm) 8.42 (s, 4 H), 8.29

(d, J = 8.8 Hz, 4 H), 6.98 (d, J = 8.8 Hz, 4 H), 4.10 - 4.00 (these are two separate triplets dt, 8 H), 1.85 - 1.79 (m, 8 H), 1.49 - 1.28 (m, 48 H), 0.93 (t, J = 7.0 Hz, 6 H), 0.48 (t, 4 H), 0.05 (s, 6 H), 0.00 (s, 12 H), -0.28 (s, 4 H); ^{13}C NMR (100 MHz, CDCl$_3$) δ 160.7, 157.0, 151.0, 143.8, 130.0, 128.9, 114.4, 68.95, 68.09, 33.7, 31.4, 29.62, 29.40-28.0 (several overlapping peaks), 26.0, 25.5, 23.9, 22.5, 18.0, 13.9, 4.1, 2.5, -0.4. LRMS (ESI) m/z 1081 ([M+1]$^+$, 100), 1065 (2), 989 HRMS (EIS) m/z calcd for C$_{64}$H$_{108}$N$_4$O$_4$Si$_3$ 1081.77511.442, found 1081.7797.

Anal. Calcd for C$_{64}$H$_{108}$N$_4$O$_4$Si$_3$: C, 71.08; H, 10.06; N, 5.18; Found: C, 71.02; H, 10, 04; N, 5.04.

1,27-Bis-[4-(5-octyloxypyrimidin-2-yl)phenoxy]-12,12,14,14,16,16-hexamethyl-12,14,16-trisilaheptacosane (QL40-8). The procedure described for the synthesis of **QL40-5** was repeated with **2-8** (0.41 g, 1.33 mmol) and 1,27-dibromo-12,12,14,14,16,16-hexamethyl-12,14,16-trisilaheptacosane (0.305 g, 0.455 mmol) The crude product was purified by flash chromatography on silica gel (3:1 hexane/EtOAc) to give **QL40-8** as a white solid (0.45 g, 67%) recrystallization from ethanol: ^{1}H NMR (400 MHz, CDCl$_3$) δ (ppm) 8.42 (s, 4 H), 8.28 (d, J = 9.0 Hz, 4H), 6.98 (d, J = 8.8 Hz, 4 H), 4.15 - 3.92 (these are two separate triplets dt, 8 H), 1.85 - 1.81 (m, 8 H), 1.51 - 1.22 (m, 52 H), 0.92 (t, J = 7.0 Hz, 6 H),), 0.47 (t, 4 H), 0.05 (s, 6 H), 0.00 (s, 12 H), -0.28 (s, 4 H); ^{13}C NMR (100 MHz, CDCl$_3$) δ 160.7, 157.0, 151.0, 143.8, 129.9, 128.9, 114.4, 68.9, 68.0, 33.7, 31.4, 29.62, 29.40-28.0 (several overlapping peaks), 26.0, 25.5, 23.9, 22.5, 18.0, 13.9, 4.1, 2.5, -0.4. LRMS (ESI) m/z 1110 ([M+1]$^+$,18) 1094 (94), 1093 (100), 998 (14), 997 (17), 809 (19), 793 (19), 639 (21), 583 (20) HRMS (EIS) m/z calcd for C$_{66}$H$_{113}$N$_4$O$_4$Si$_3$ 1109.8064, found 1109.8049.

Anal. Calcd for C$_{66}$H$_{113}$N$_4$O$_4$Si$_3$: C, 71.36; H, 10.25; N, 5.04; Found: C, 71.74; H, 10, 24; N, 5.08.

1,27-Bis-[4-(5-nonyloxypyrimidin-2-yl)phenoxy]-12,12,14,14,16,16-hexamethyl-12,14,16-trisilaheptacosane (QL40-9). The procedure described for the synthesis of **QL40-5** was repeated with **2-9** (0.21 g, 0.670 mmol) and 1,27-dibromo-12,12,14,14,16,16-hexamethyl-12,14,16-trisilaheptacosane (0.15 g, 0.223 mmol) The crude product was purified by flash chromatography on silica gel (3:1 hexane/EtOAc) to give **QL40-9** as a white solid (0.17 g, 68%) recrystallization from ethanol: ^{1}H NMR (400 MHz, CDCl$_3$) δ (ppm) 8.42 (s, 4 H), 8.28 (d, J = 9.1 Hz, 4 H), 6.98 (d, J = 9.1 Hz, 4 H), 4.15 - 3.92 (these are two separate triplets dt, 8 H), 1.85 - 1.81 (m, 8 H), 1.51 - 1.22 (m, 56 H), 0.92 (t, J = 6.9 Hz, 6 H),), 0.47 (t, 4 H), 0.05 (s, 6 H), 0.00 (s, 12 H), -0.28 (s, 4 H); ^{13}C NMR (100 MHz, CDCl$_3$) δ 160.68, 153.29, 151.05, 143.83, 135.99, 128.95, 114.42, 68.93, 68.08, 33.72, 31.85, 29.63-28.08 (several overlapping peaks), 26.06, 25.52, 23.98, 22.66, 19.18, 14.11, 4.10, 2.53, -0.43. LRMS (ESI) *m/z* 1137 ([M+1]$^+$,100), 1021 (20), 1011 (3), 919 (7), 635 (2) ,597 (2) HRMS (EIS) *m/z* calcd for C$_{68}$H$_{116}$N$_4$O$_4$Si$_3$ 1137.8377, found 1137.8348.

Anal. Calcd for C$_{68}$H$_{116}$N$_4$O$_4$Si$_3$: C, 71.77; H, 10.27; N, 4.92; Found: C, 72.02; H, 10, 22; N, 5.04.

1,27-Bis-[4-(5-decyloxypyrimidin-2-yl)phenoxy]-12,12,14,14,16,16-hexamethyl-12,14,16-trisilaheptacosane (QL40-10). The procedure described for the synthesis of **QL40-5** was repeated with **2-10** (0.21 g, 0.669 mmol) and 1,27-dibromo-12,12,14,14,16,16-hexamethyl-12,14,16-trisilaheptacosane (0.15 g, 0.223 mmol) The crude product was purified by flash chromatography on silica gel (3:1 hexane/EtOAc) to give **QL40-10** as a white solid (0.30 g, 78%) recrystallization from ethanol: ^{1}H NMR (400 MHz, CDCl$_3$) δ (ppm) 8.42 (s, 4 H), 8.28 (d, J = 7. 9 Hz, 4H), 6.98 (d, J = 8. 1 Hz, 4 H), 4.15 - 3.92 (these are two separate triplets dt, 8 H), 1.81 - 1.85 (m, 8 H), 1.51 - 1.22 (m, 60 H), 0.92 (t, J = 6. 4 Hz, 6 H),), 0.47 (t, 4 H), 0.05 (s, 6 H), 0.00 (s, 12 H), -0.28 (s, 4 H): ^{13}C NMR (100 MHz, CDCl$_3$) δ 160.68, 153.29, 151.05,

143.83, 135.99, 128.95, 114.42, 68.93, 68.08, 33.72, 31.85, 29.63-28.08 (several overlapping peaks), 26.06, 25.52, 23.98, 22.66, 19.18, 14.11, 4.10, 2.53, -0.43. LRMS (ESI) *m/z* 1164 (8), 1149 (90), 1148 (100), 1125 (20), 1124 (31), 938 (35), 922 (17), 677 (20), 611 (12) HRMS (EIS) *m/z* calcd for $C_{70}H_{120}N_4O_4Si_3$ 1165.8690, found 1165.8720.

Anal. Calcd for $C_{70}H_{120}N_4O_4Si_3$: C, 72.11; H, 10.37; N, 4.81; Found: C, 71.98; H, 30, 04; N, 4.84.

3.2 Reference

1- Zhang, Y.; O'Callaghan, M. J.; Walker, C.; Baumeister, U.; Tschierske, C. *Chem. Mater*. **2010**, 22, 2869.

Chapter 4. Conclusions and Future Work

The first goal of this thesis was to test a hypothesis regarding the effect of carbosilane nanosegregation on the 'de Vries-like' properties of smectic liquid crystals, based on the previous findings of the Lemieux group. Those findings indicated that correlation with carbosilane end-group mesogens may produce a significant amount of free volume in the hydrocarbon sub-layer. An additional goal of this thesis was further understanding of the origin of 'de Vries-like' behavior in carbosilane end-group mesogens.

In this thesis, two new homologous series of carbosilane liquid-crystal dimers (**QL40-n**) and monomers (**QL39-n**) with tricarbosilane spacers and end-group, respectively were synthesized. The POM and X-ray data indicate that, in **QL40-n** series, orthogonal SmA and SmX phases are formed, whereas **QL39-n** form a tilted SmC phase only. The fact that the SmA phase is not observed in **QL39-n** suggests that the dimers and monomers have different properties. The evidence suggests that the carbosilane segment in the dimers **QL40-n** has a smaller cross-section on time average than in the monomers**QL39-n**, which is consistent with our hypothesis.

Further studies will seek to validate these results by restoring the 'de Vries-like' behavior in the **QL41-n** series using a laterally bulky tricarbosilane spacer in which R = CH$_2$SiMe$_3$.

CH_3-$(CH_2)_n$—O—[pyrimidine]—[phenyl]—O—$(CH_2)_{11}$—Si—Si—Si—$(CH_2)_{11}$—O—[phenyl]—[pyrimidine]—O-$(CH_2)_n$-CH_3
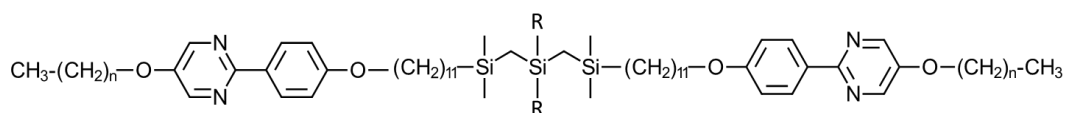
QL41-n

Appendix 1. ^{1}H NMR Spectra of Novel Liquid Crystals
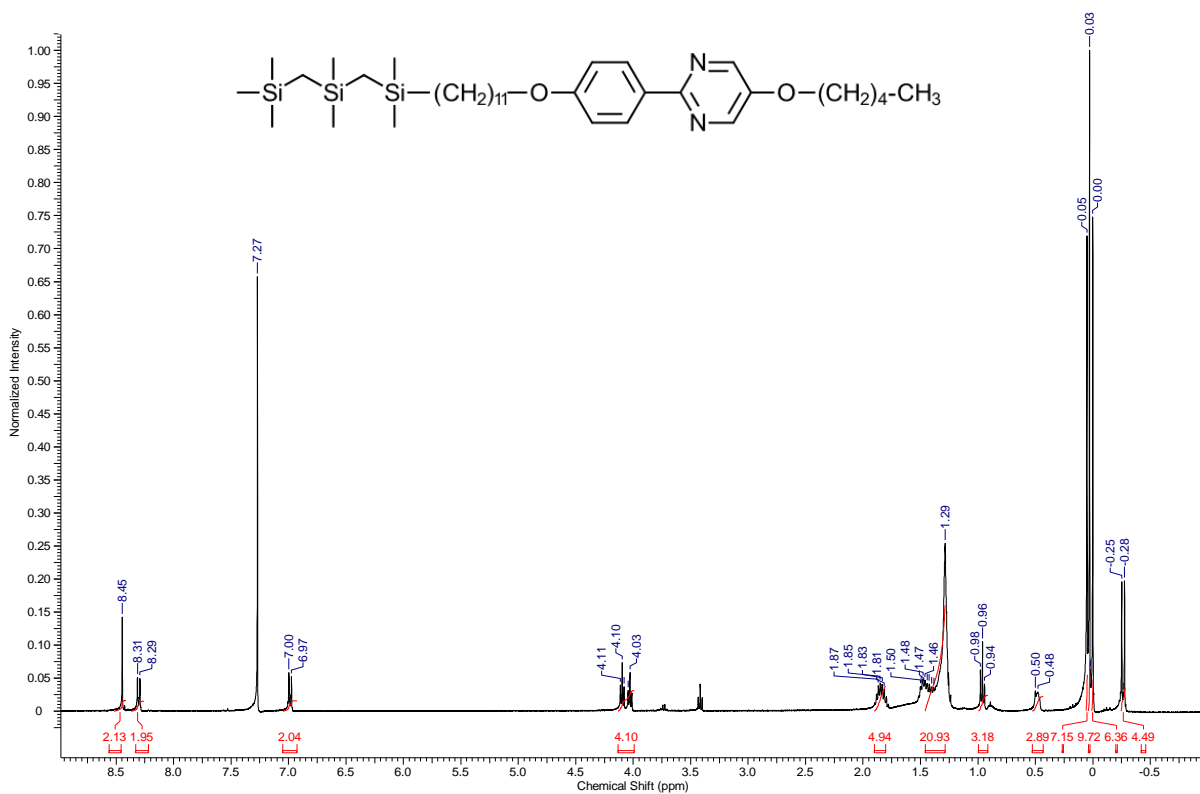
Figure A1-1: 400 MHz ^{1}H NMR spectrum of **QL39-5**
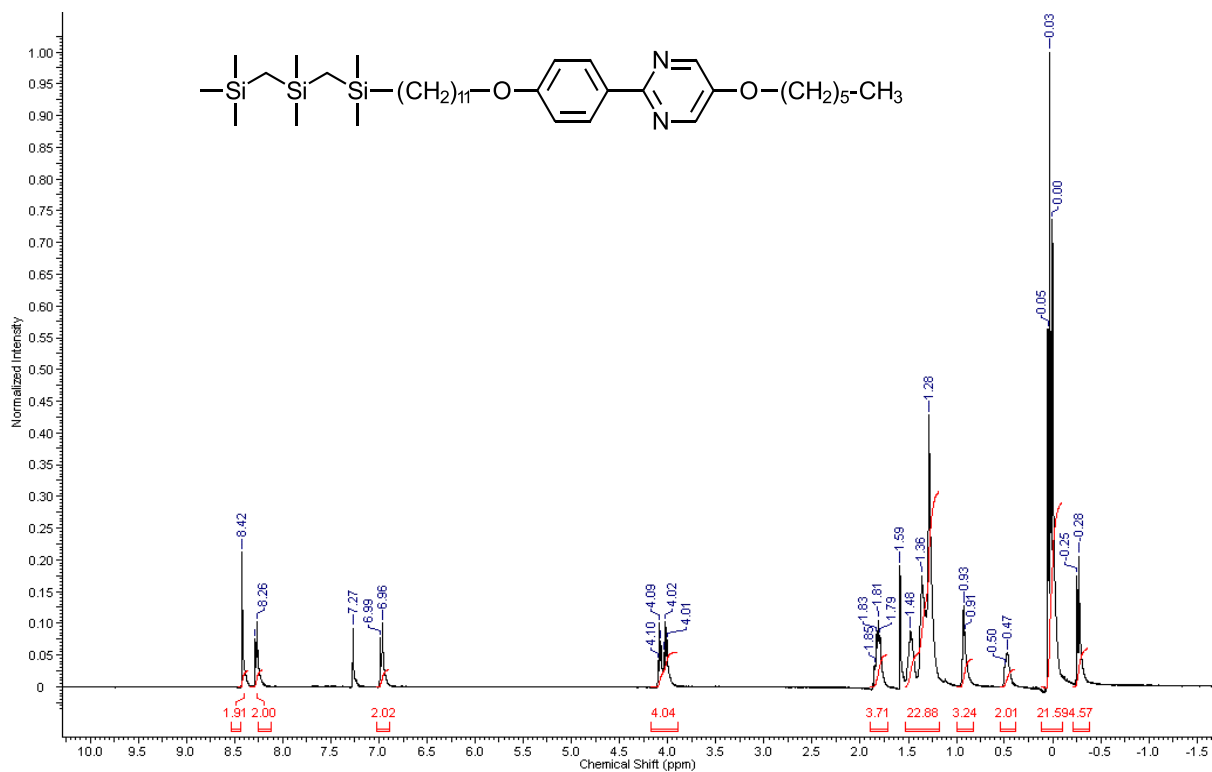
Figure A1-2: 400 MHz ^{1}H NMR spectrum of **QL39-6**
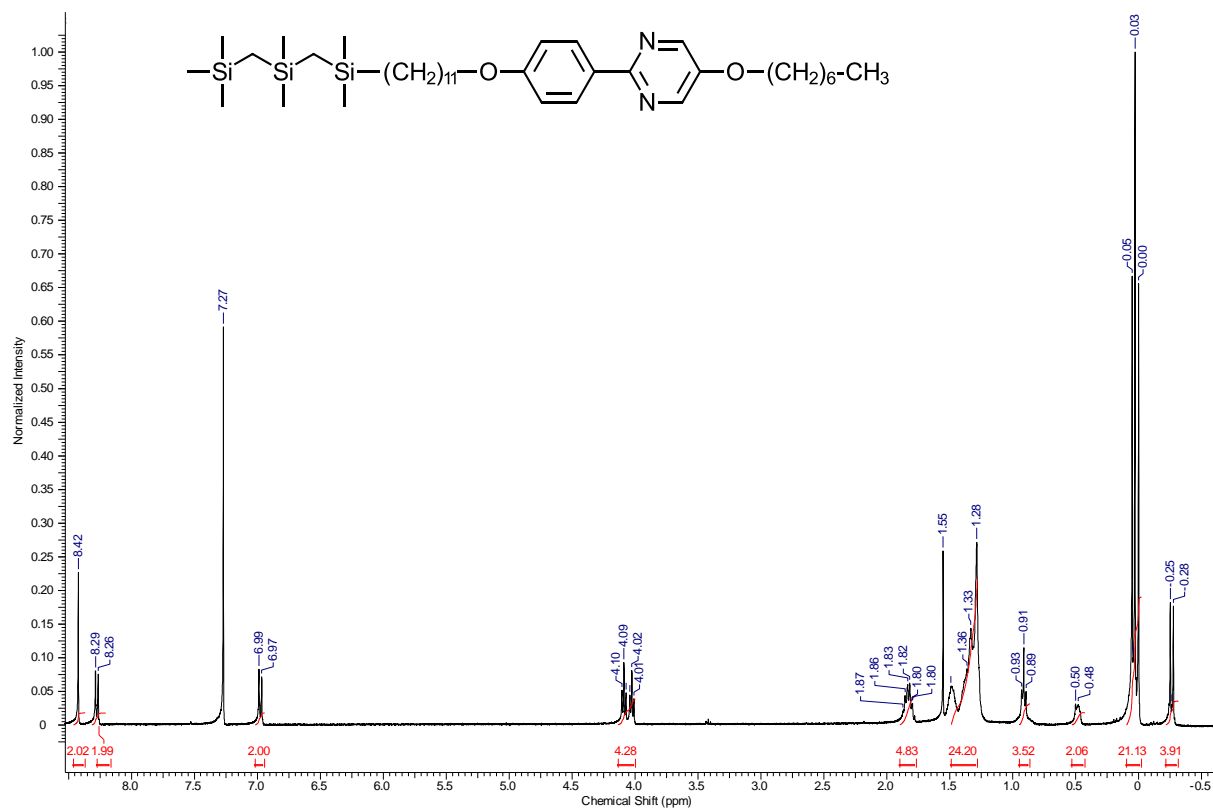
Figure A1-3: 400 MHz ¹H NMR spectrum of **QL39-7**
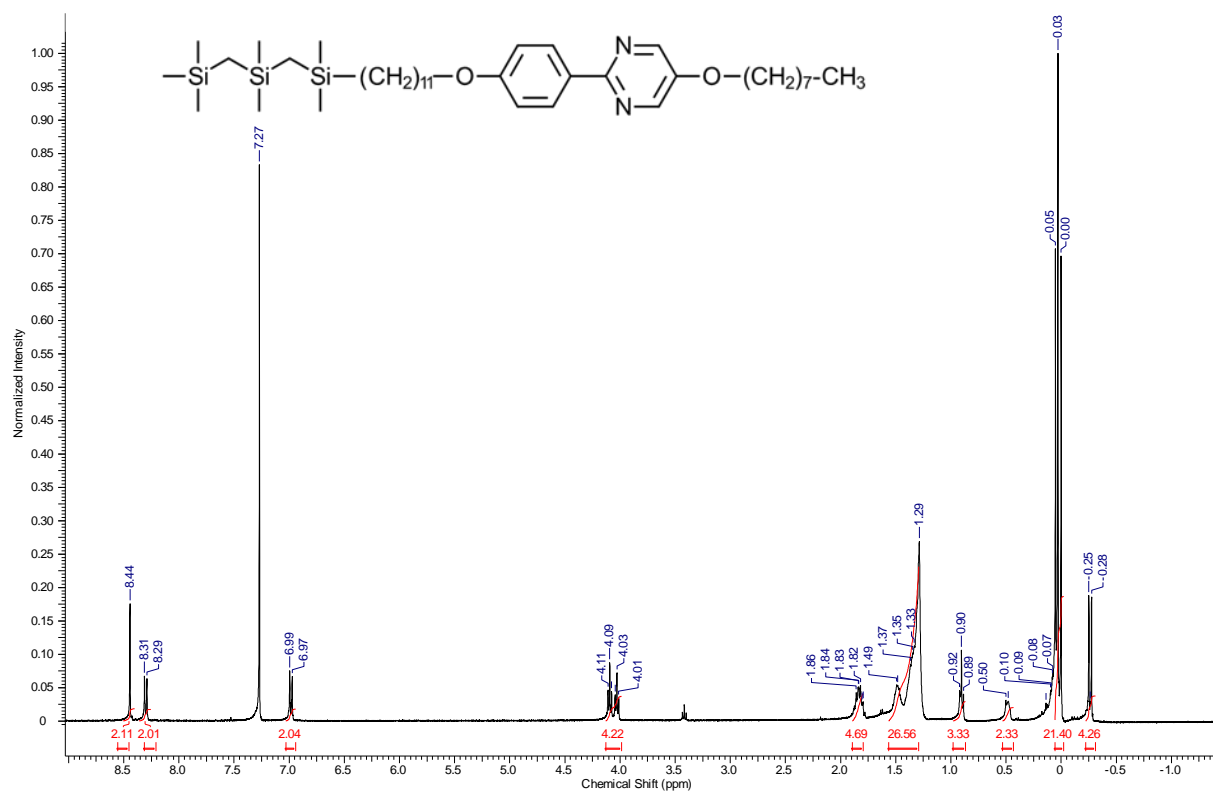
Figure A1-4: 400 MHz ¹H NMR spectrum of **QL39-8**
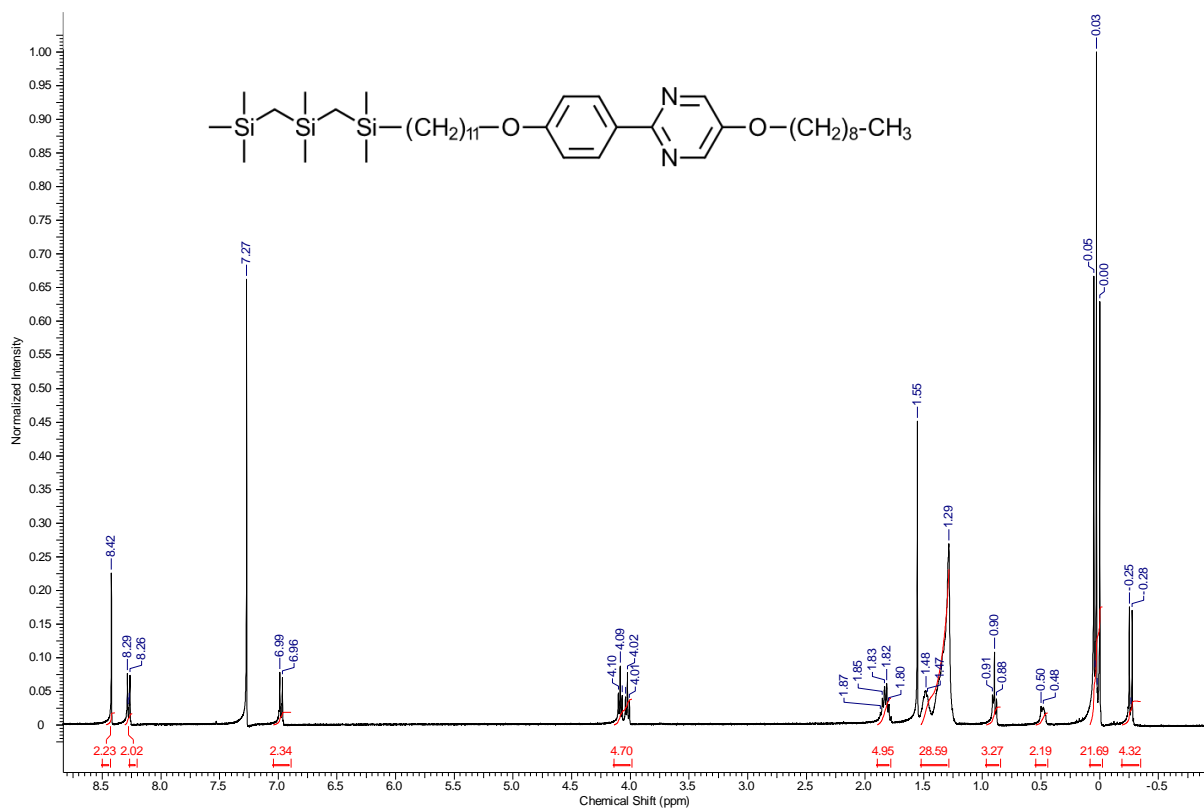
Figure A1-5: 400 MHz ^{1}H NMR spectrum of **QL39-9**
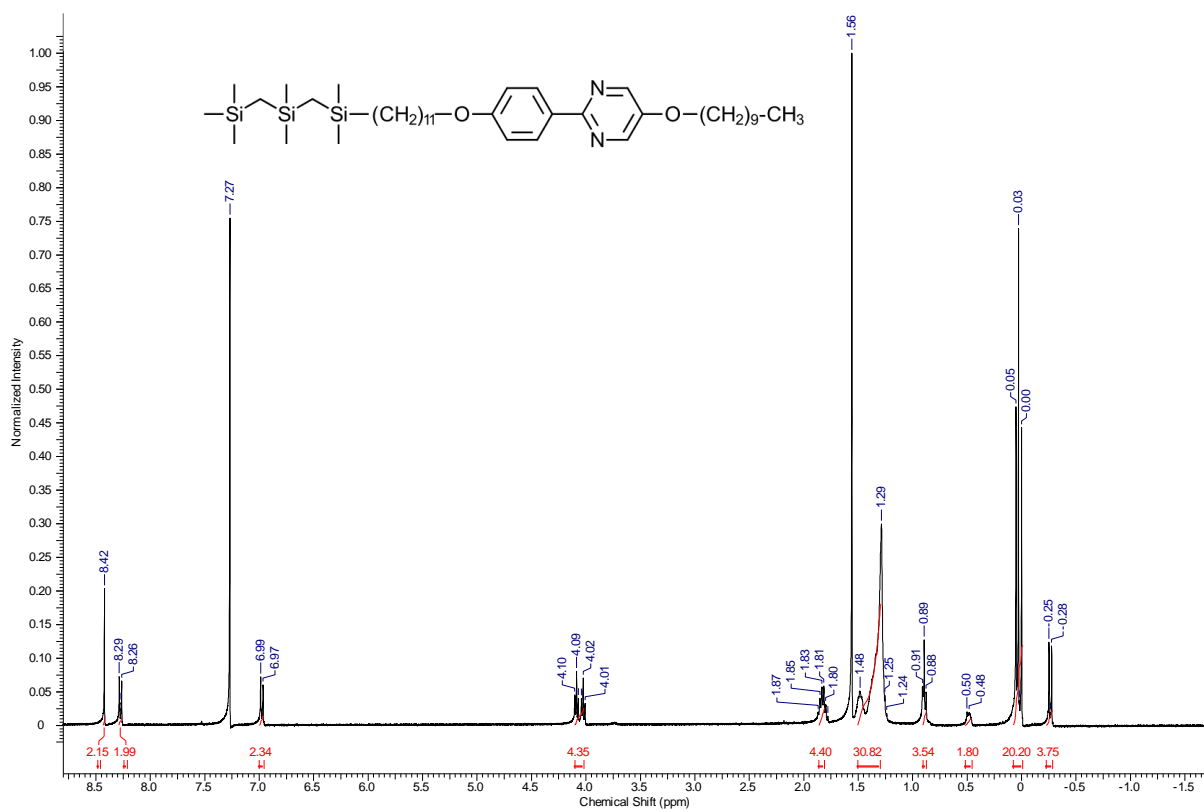
Figure A1-6: 400 MHz ^{1}H NMR spectrum of **QL39-10**
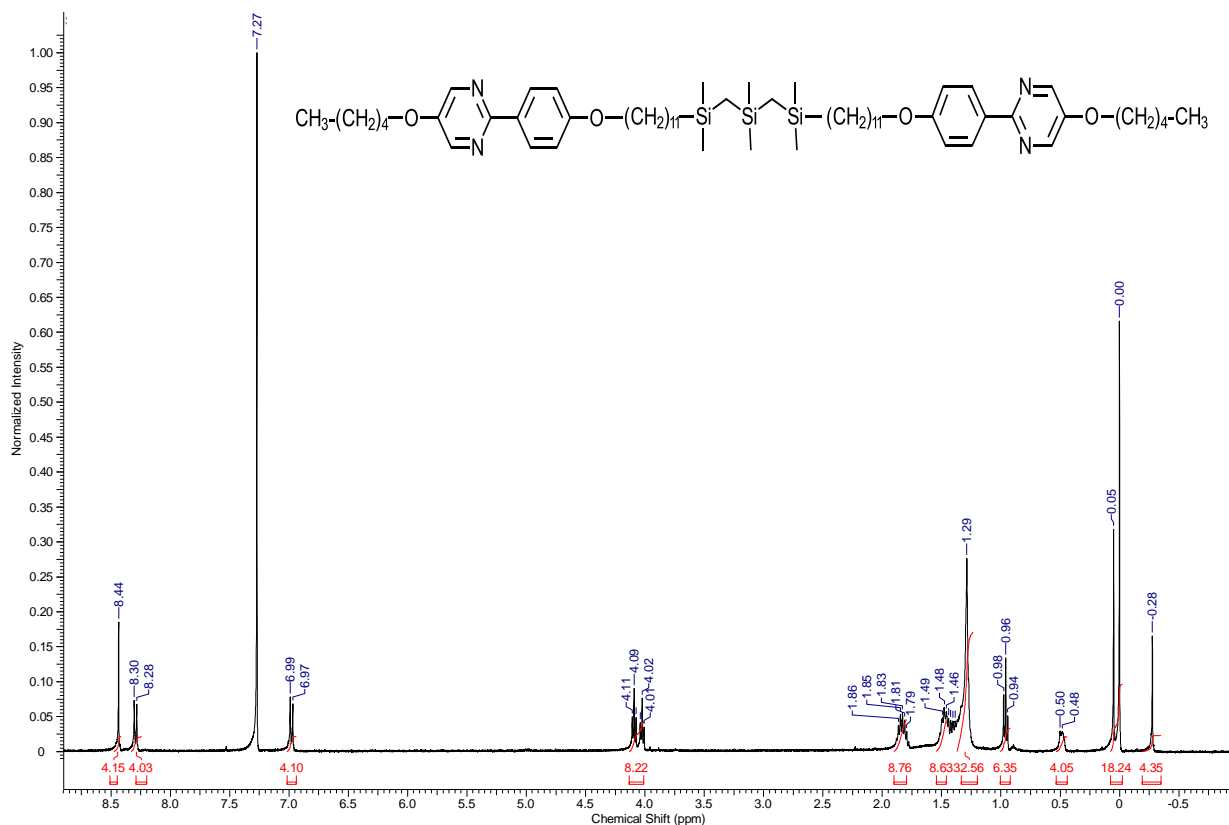
Figure A1-7: 400 MHz ^{1}H NMR spectrum of **QL40-5**
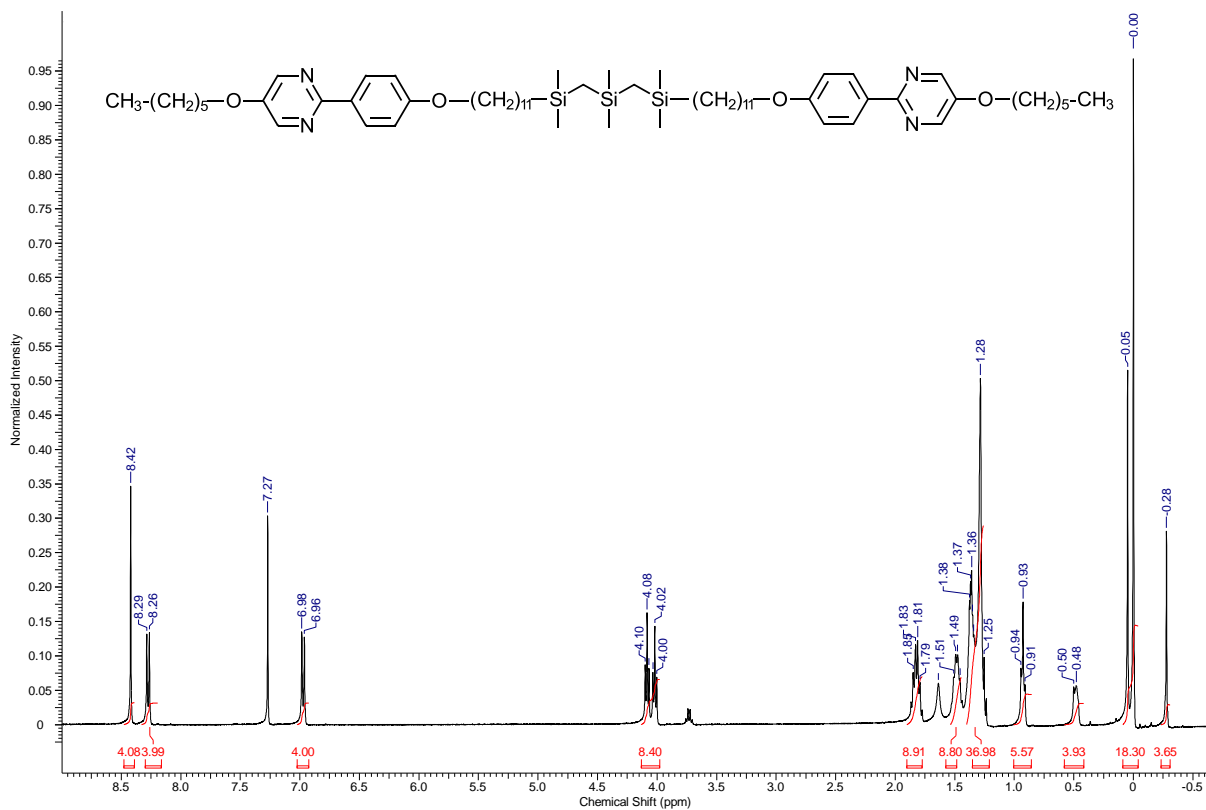
Figure A1-8: 400 MHz ^{1}H NMR spectrum of **QL40-6**
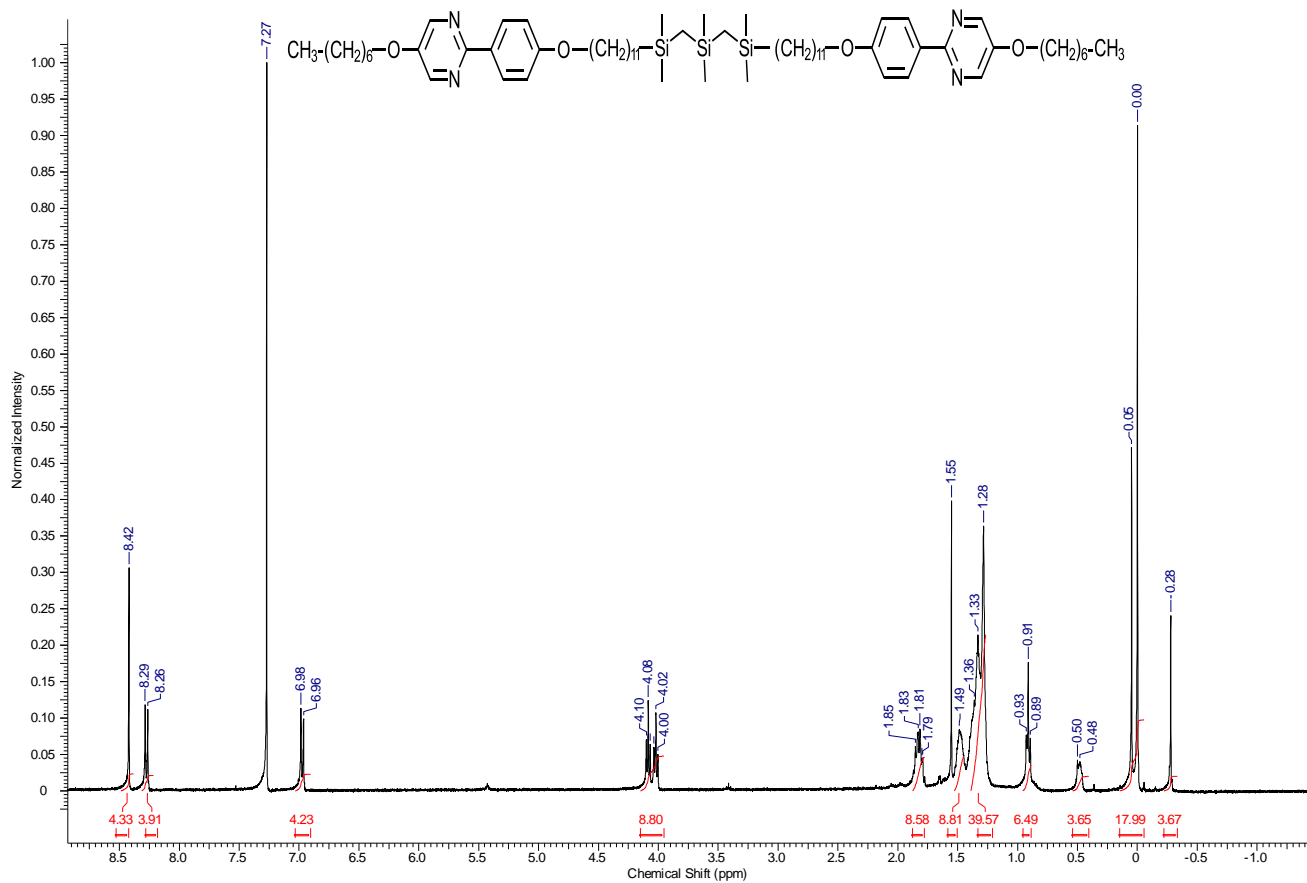
Figure A1-9: 400 MHz ^{1}H NMR spectrum of **QL40-7**
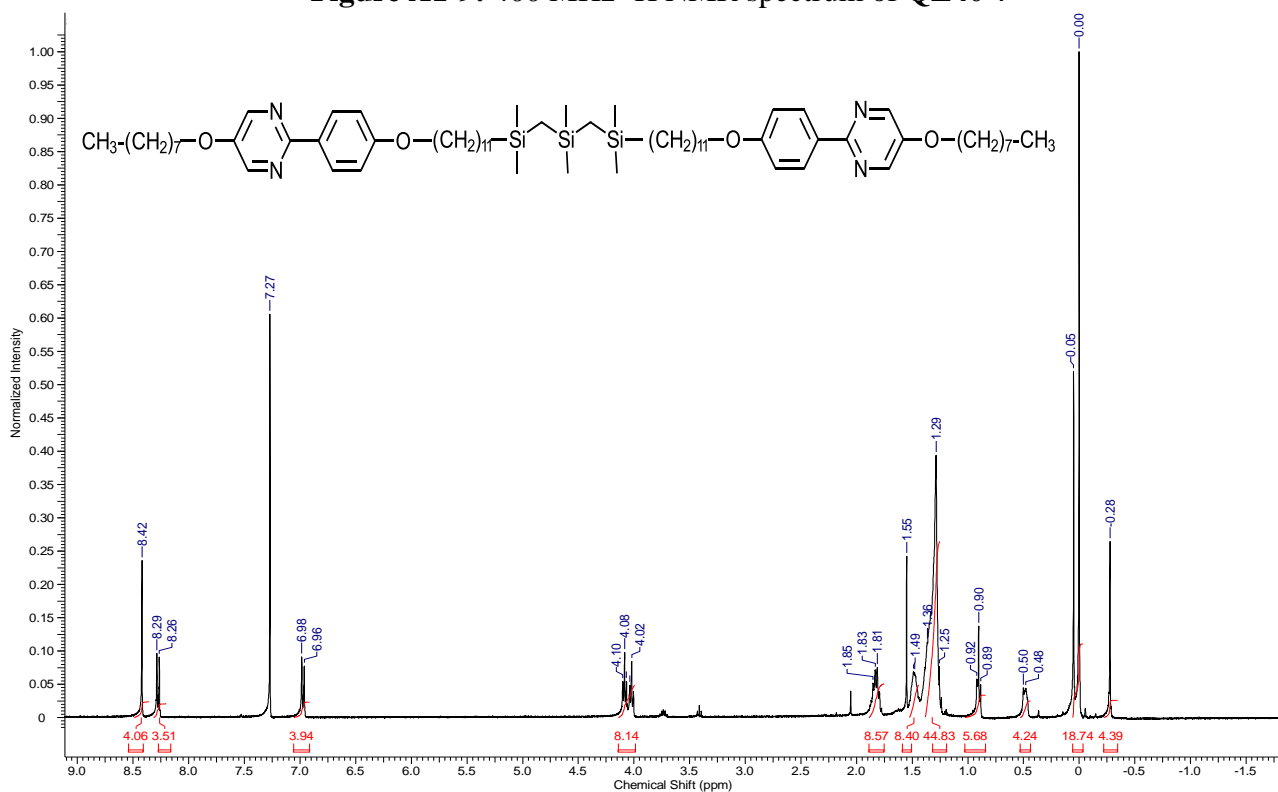
Figure A1-10: 400 MHz ^{1}H NMR spectrum of **QL40-8**

59
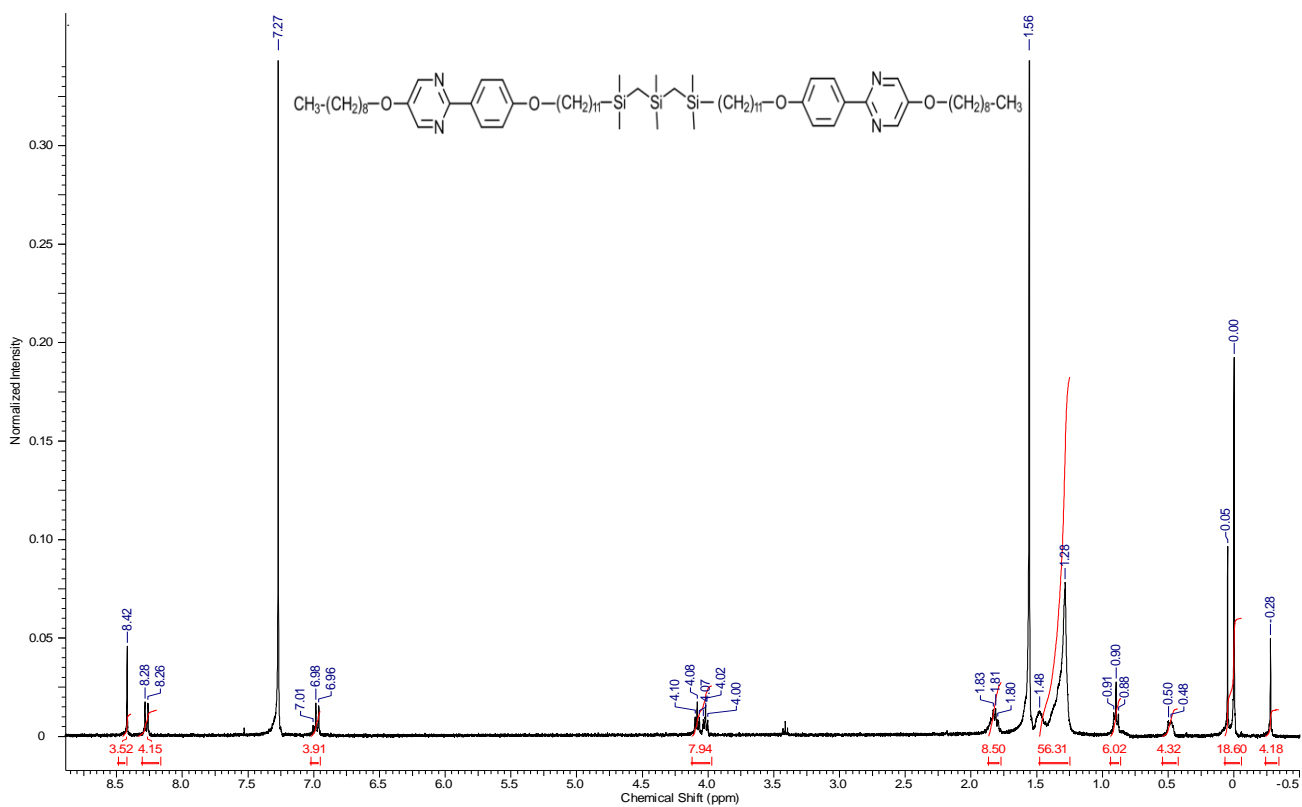
Figure A1-11: 400 MHz ^{1}H NMR spectrum of **QL40-9**
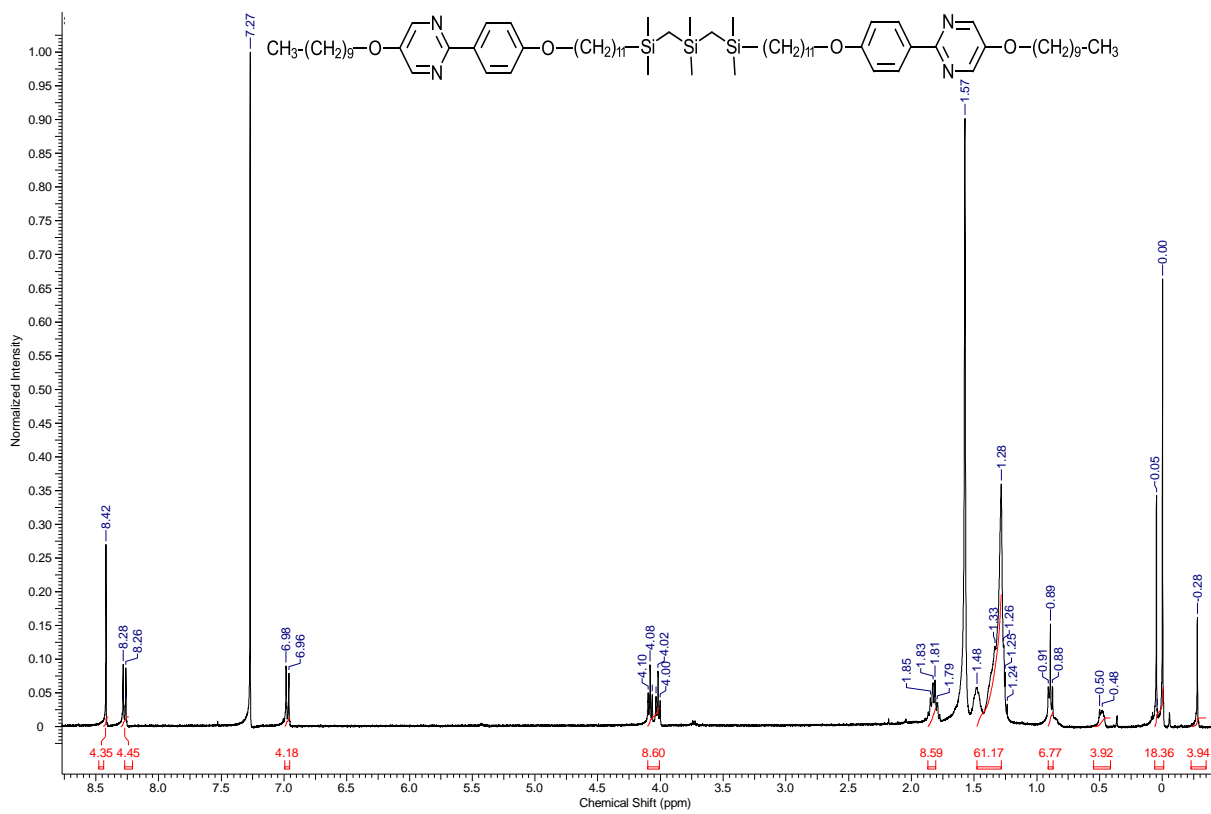
Figure A1-12: 400 MHz ^{1}H NMR spectrum of **QL40-10**

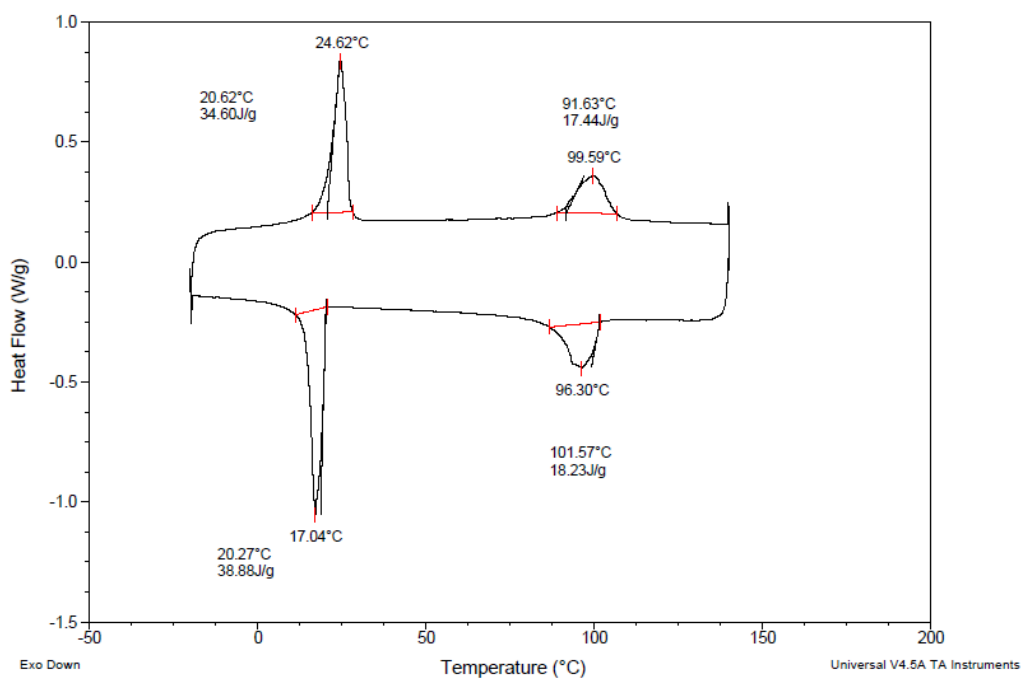# Appendix 2. DSC Profiles of Liquid Crystals
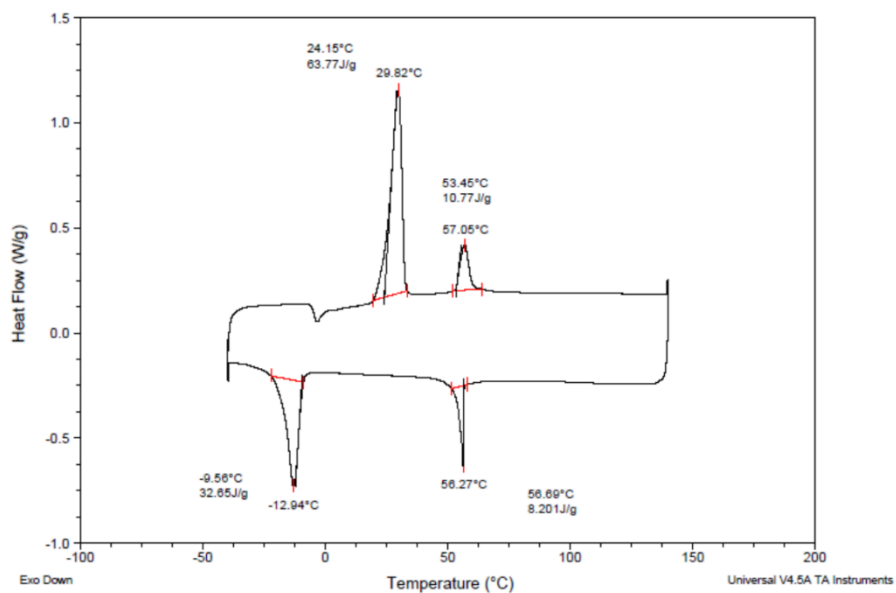
Figure A2-1: DSC profile for compound **QL39-5** taken at a scan rate of 5K/min.
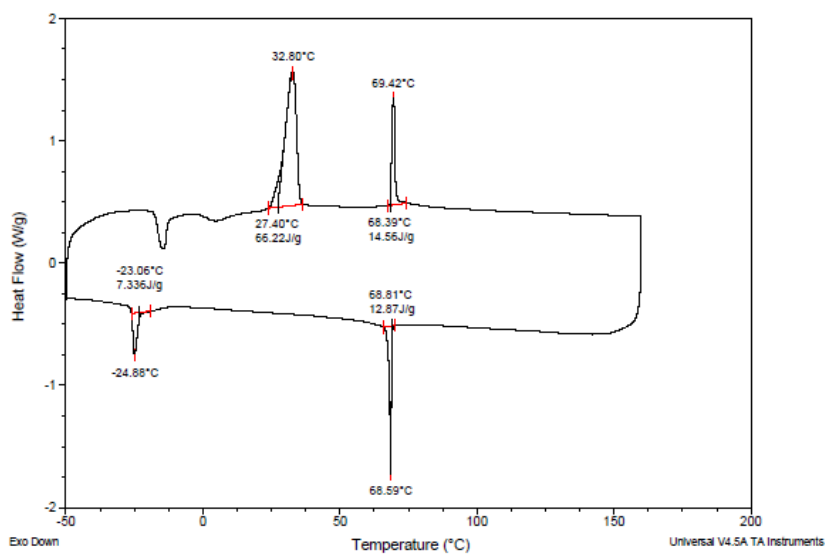
**Figure A2-2**: DSC profile for compound **QL39-6** taken at a scan rate of 5K/min.
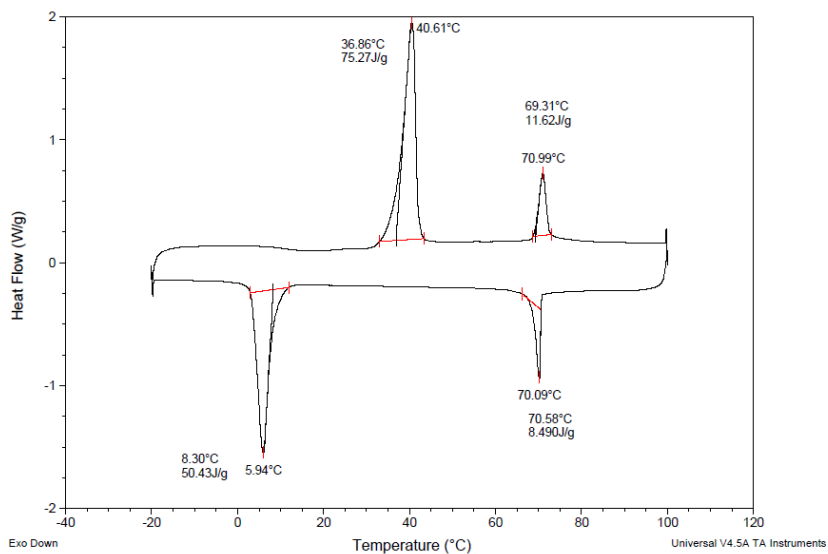
Figure A2-3: DSC profile for compound **QL39-7** taken at a scan rate of 5K/min.
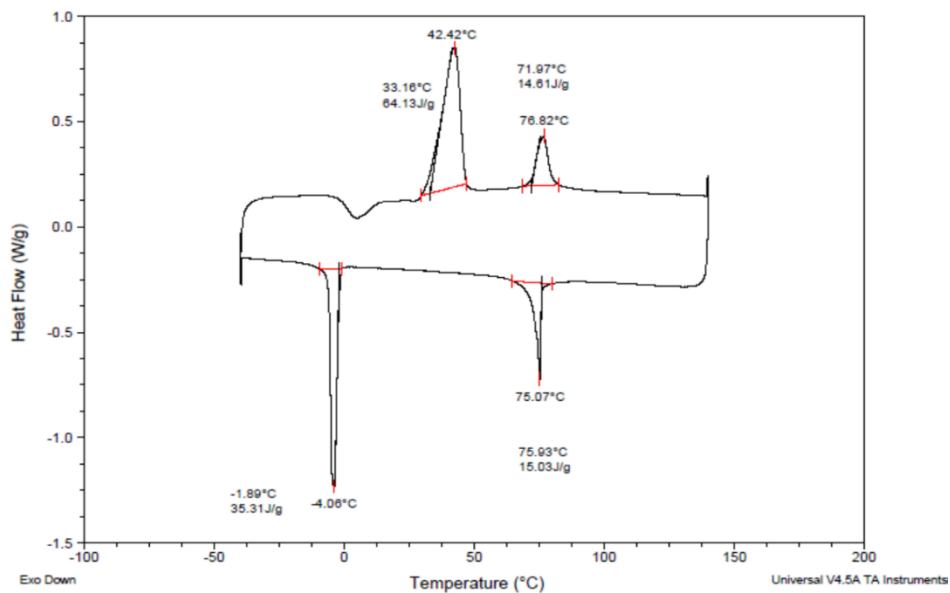

Figure A2-4: DSC profile for compound **QL39-8** taken at a scan rate of 5K/min.
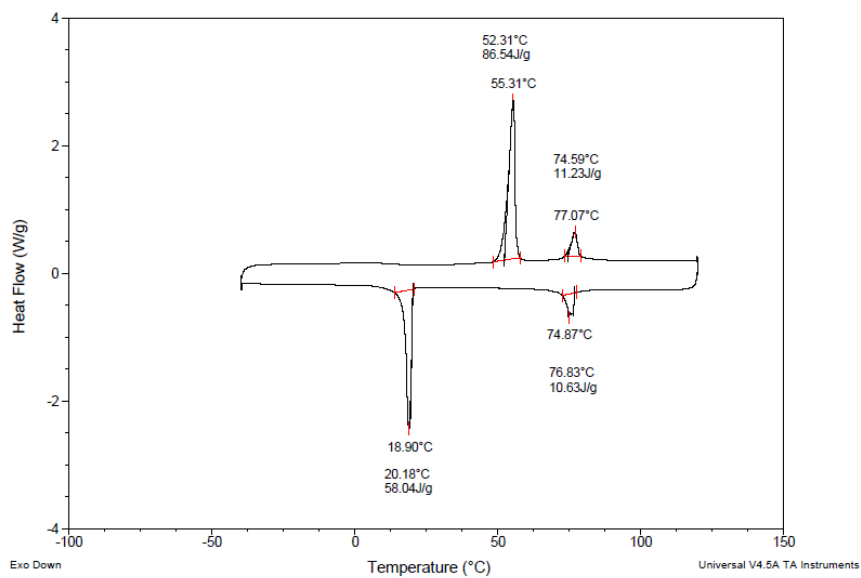
Figure A2-5: DSC profile for compound **QL39-9** taken at a scan rate of 5K/min.
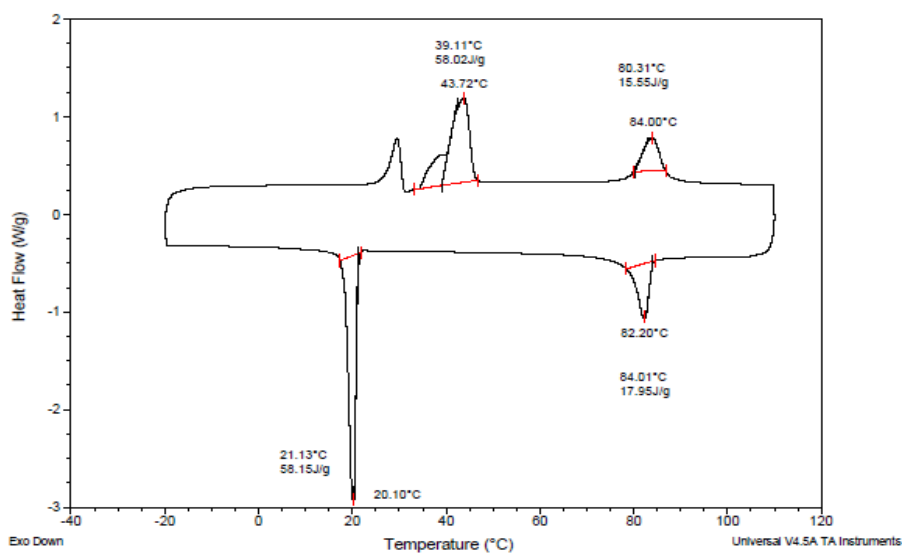
Figure A2-6: DSC profile for compound **QL39-10** taken at a scan rate of 5K/min.
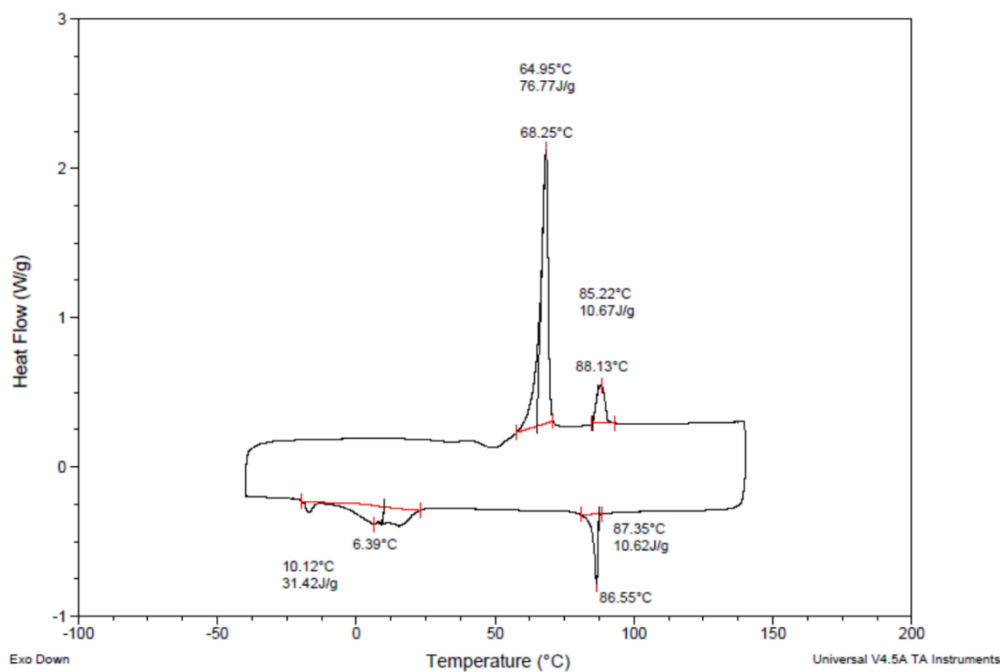
Figure A2-7: DSC profile for compound **QL40-5** taken at a scan rate of 5K/min.
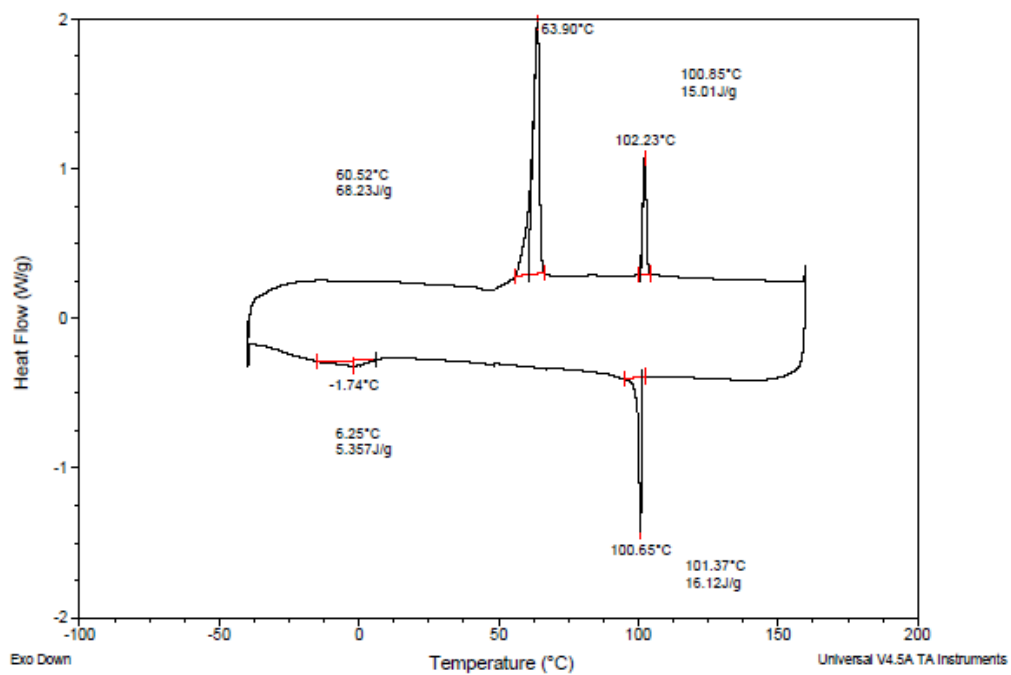
Figure A2-8: DSC profile for compound **QL40-6** taken at a scan rate of 5K/min.
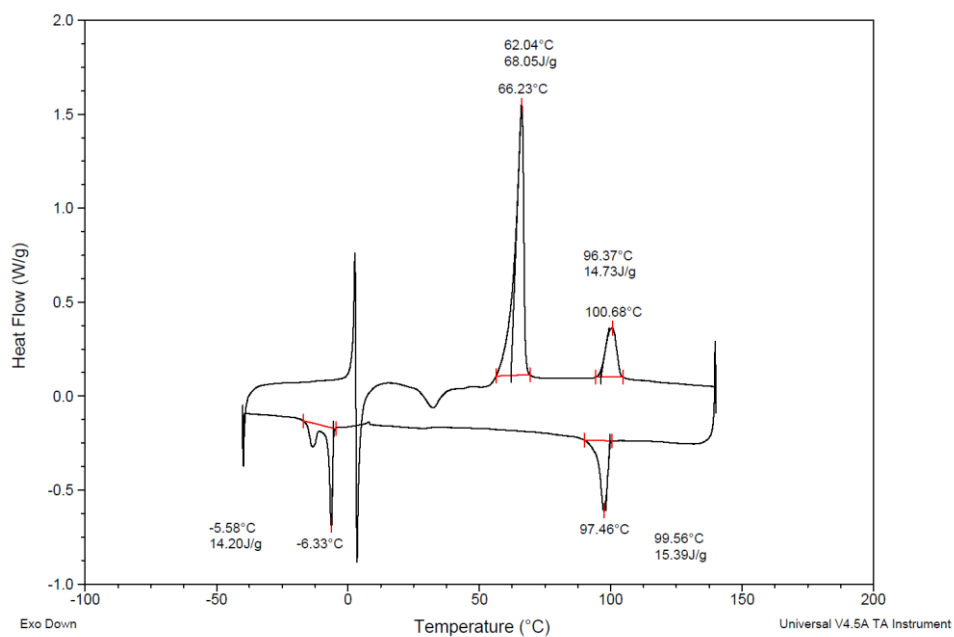
Figure A2-9: DSC profile for compound **QL40-7** taken at a scan rate of 5K/min.
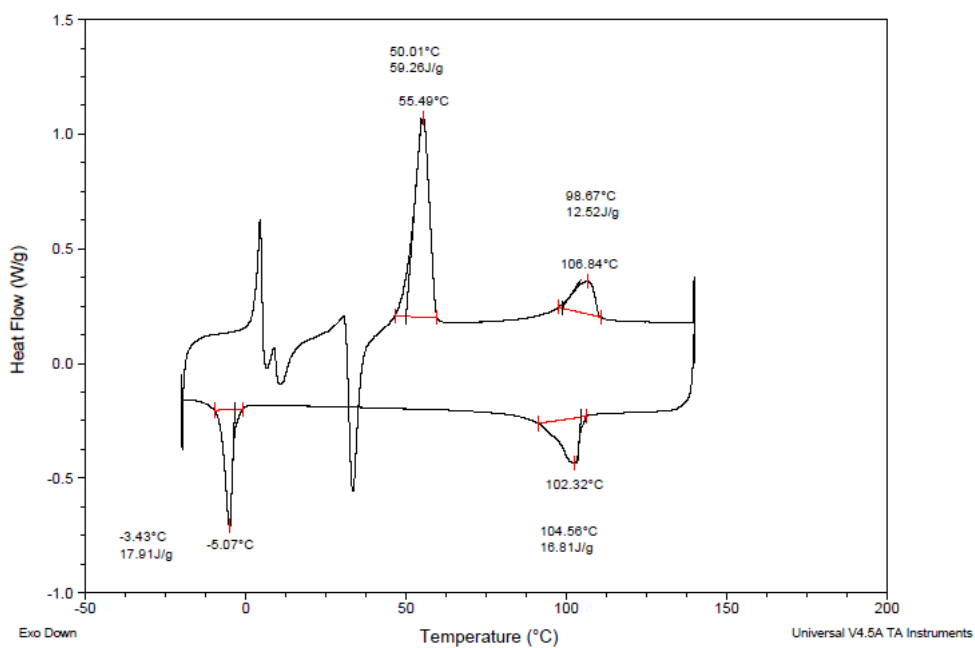
Figure A2-10: DSC profile for compound **QL40-8** taken at a scan rate of 5K/min.
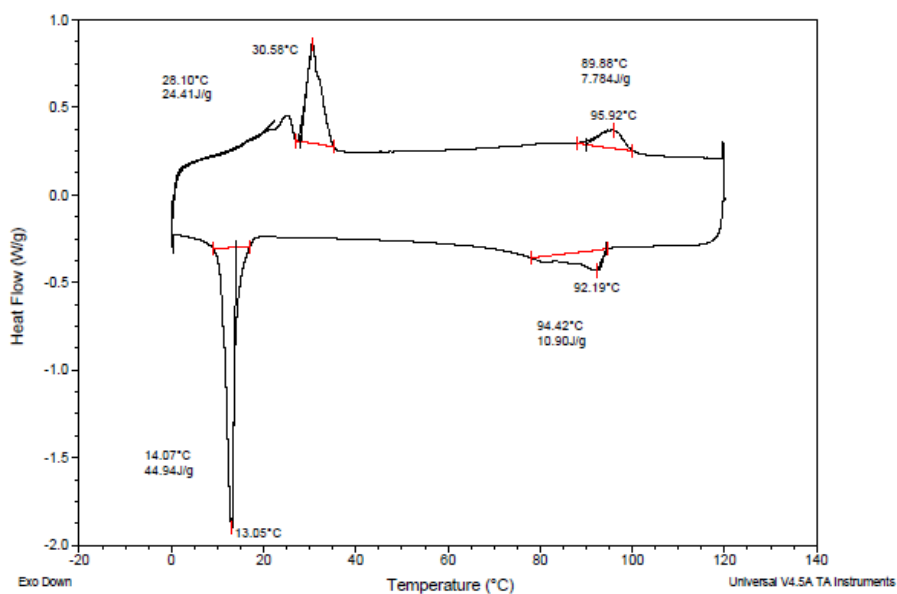
Figure A2-11: DSC profile for compound **QL40-9** taken at a scan rate of 5K/min.

Figure A2-12: DSC profile for compound **QL40-10** taken at a scan rate of 5K/min.

Appendix 3. Textures of Liquid Crystals by Polarized Microscopy
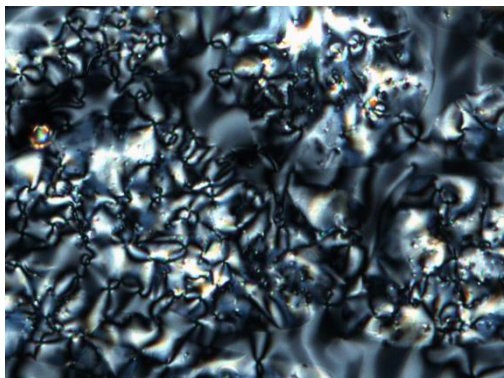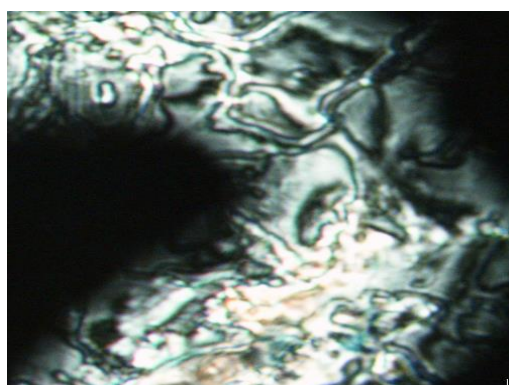

Figure A3-1: Textures of compound **QL39-5** observed by polarized microscopy on cooling: in the SmC phase at 42 °C.
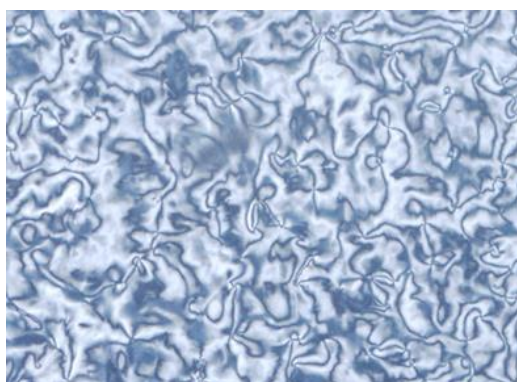
Figure A3-2: Textures of compound **QL39-6** observed by polarized microscopy on cooling: in the SmC phase at 70 °C.
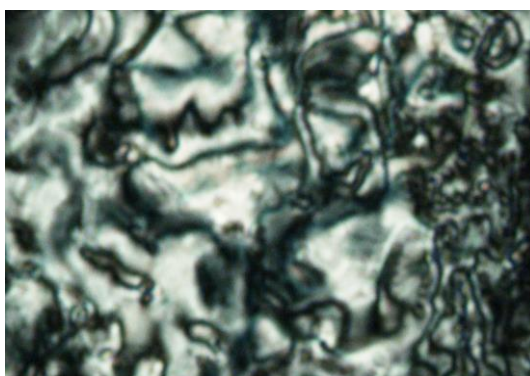
Figure A3-3: Textures of compound **QL39-7** observed by polarized microscopy on cooling: in the SmC phase at 68 °C.
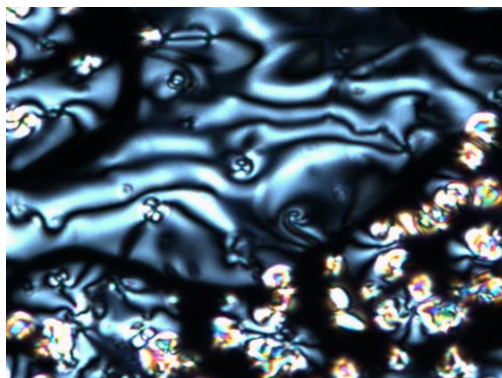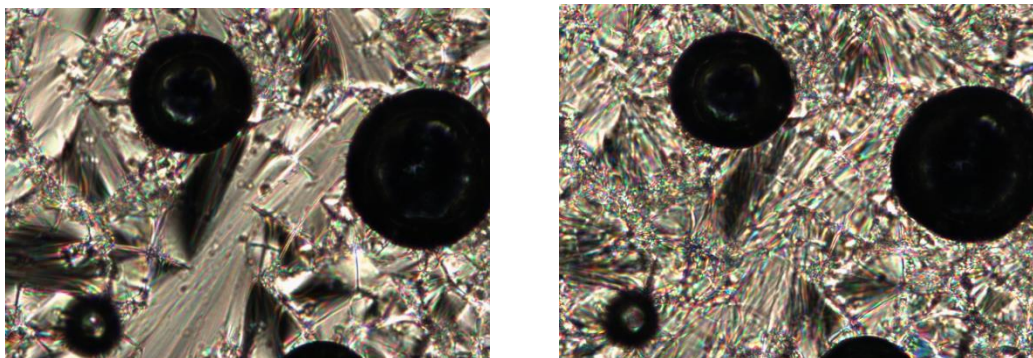
Figure A3-4: Textures of compound **QL39-8** observed by polarized microscopy on cooling: in the SmC phase at 69 °C.
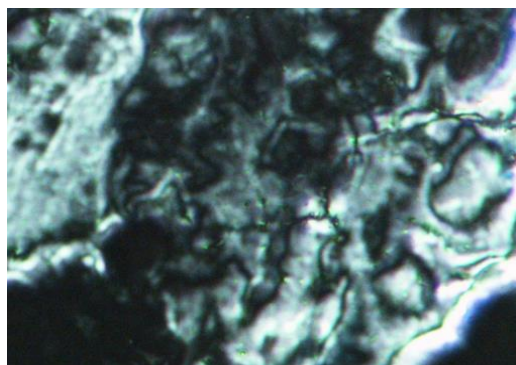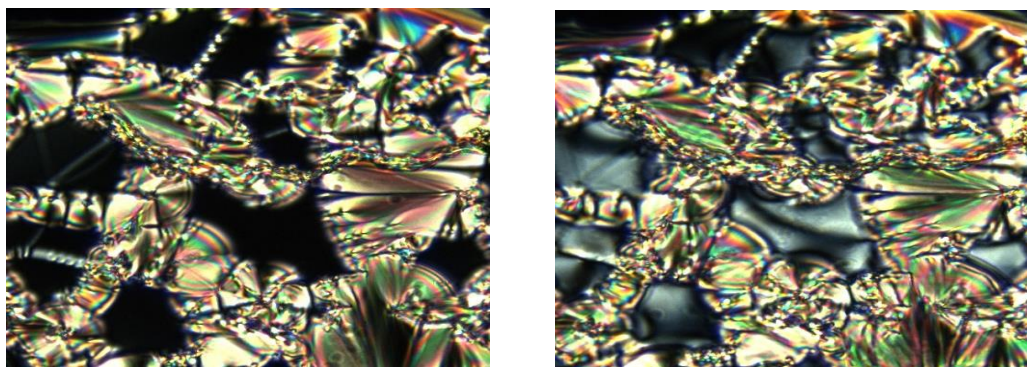

Figure A3-5: Textures of compound **QL39-9** observed by polarized microscopy on cooling: in the SmC phase at 66 °C.
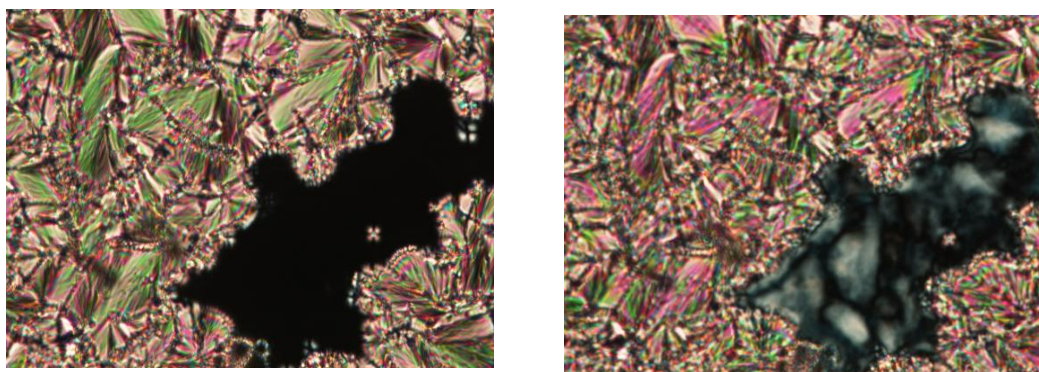

Figure A3-6: Textures of compound **QL39-10** observed by polarized microscopy on cooling: in the SmC phase at 80 °C.
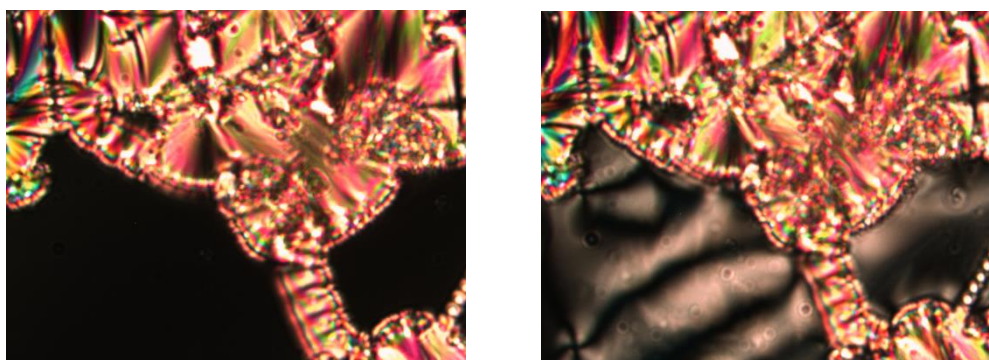
Figure A3-7: Textures of compound **QL40-5** observed by polarized microscopy on cooling in the SmA at 85 $^\circ$C on cooling (left) and the SmX phase at 70 $^\circ$C (right) (200X Magnification).
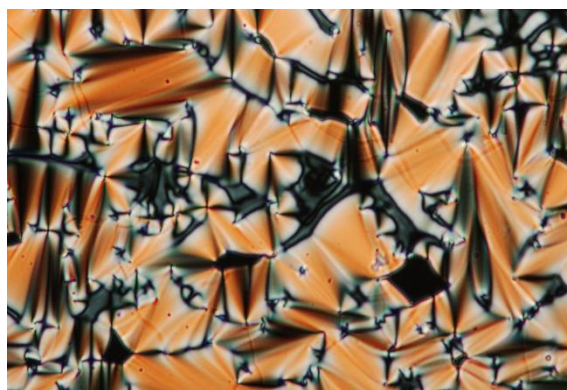

Figure A3-8: Textures of compound **QL40-6** observed by polarized microscopy on cooling: in the SmA phase at 91 $^\circ$C (left) and in the SmX phase at 74 $^\circ$C (right) (200X Magnification).

Figure A3-9: Textures of compound **QL40-7** observed by polarized microscopy on cooling: in the SmA phase at 90 $^\circ$C (left) and in the interfere SmX phase at 75°C (right) (200X Magnification).

Figure A3-10: Textures of compound **QL40-8** observed by polarized microscopy on cooling: in the SmA phase at 95 °C (left) and in the SmX phase at 93 °C (right) (200X Magnification).
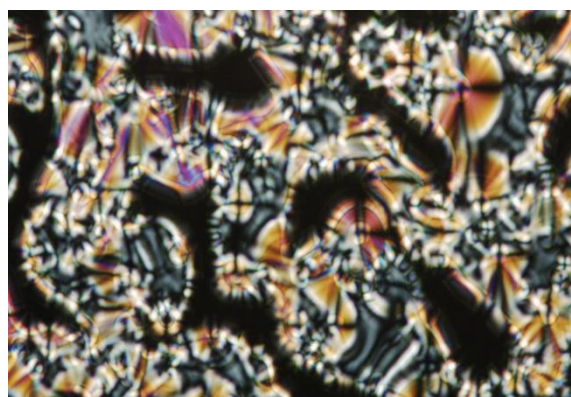

Figure A3-11: Textures of compound **QL40-9** observed by polarized microscopy on cooling: in the SmA phase and the interfere SmA phase at 85 °C (200X Magnification).

Figure A3-12: Textures of compound **QL40-10** observed by polarized microscopy on cooling: in the SmA phase and the interfere SmA phase at 90 °C (200X Magnification).